Supporting Information

Oxygen Vacancy-Enhanced Hydrogen Spillover on Bifunctional PdFe/TiO_{2-x} Catalyst for Highly Selective Direct Hydrodeoxygenation of Carbonyl Compounds

Chaofan Deng and Chun Cai *

School of Chemistry and Chemical Engineering, Nanjing University of Science and Technology, Nanjing, Jiangsu 210094, P. R. China

*Corresponding author: Chun Cai

Email: c.cai@njust.edu.cn

Table of Contents

1. Characterization methods

The XRD of the sample was taken on a Bruker D2 PHASER X-ray diffractometer equipped with Cu Kα radiation (λ = 0.15418 nm) under 36 kV voltage and 30 mA current. And the data of the catalysts were collected from 2θ = 5-80° at a scanning rate of 5 °/min. The scanning electron microscope (SEM) used in this work is a su8220 model, equipped with a copper cathode as the emission source with a test voltage of 15 kV. Transmission electron microscopy (TEM) experiments were carried out using a JEOL JEM-2100F, and measurements were made at the Spectrum X-MaxN 80T IE250. The XPS measurements were carried out on an ESCALAB 250Xi spectrometer (Thermo Scientific, USA) equipped with a pass energy of 30 eV with a power of 100 W (10 kV and 10 mA) and a mono-chromatized AlKα X-ray (hv=1486.65 eV) source. All samples were analyzed under a pressure of less than 1.0×10^{-9} Pa. Spectra were acquired through the avantage software (Version 5.979) with a step of 0.05 eV. The infrared thermal imager (Testo869) was used to take the infrared thermal image of the catalyst at a distance of 15 cm after five minutes of light to study the photothermal effect of catalyst under illumination and without external light source. The NH_3 temperature-programmed desorption (NH_3-TPD) tests for the reducing catalysts were measured with American Mac ASAP 2920, quanta-chrome instrument equipped with a thermal conductivity detector (TCD). CO_2-TPD/MS was tested with a Micromeritics asap 2920 instrument and Hiden Analytical The test condition of the sample was firstly he gas purging, holding at 300 degrees Celsius for half an hour, then cooling down to 50 degrees Celsius, switching to CO_2/He gas purging for half an hour, and finally switching to He gas, stabilizing, and then warming up to

600 degrees Celsius and connecting to mass spectrometry for detection. H_2-TPD/MS measurements were conducted using a Micromeritics ASAP 2920 instrument in combination with a Hiden Analytical system. First, the sample was purged with Ar gas at a heating rate of 10 °C/min to 300 °C and held for 30 min. The temperature was then reduced to 50 °C, followed by purging with 10% H_2/Ar gas until the baseline stabilized. Subsequently, the temperature was increased at a rate of 10 °C/min to 700 °C for analysis. The H_2-TPR/MS setup was identical to that used for H_2-TPD/MS. After purging with 10% H_2/Ar gas at 10 °C/min to 350 °C and holding for 30 min, the temperature was cooled to 50 °C, then purged with Ar gas to stabilize the baseline before heating to 800 °C. BET analysis was tested using a Micromeritics-3Flex instrument from Mac, USA. Raman spectra were measured using a French horiba HR evolution. Determination using ICP was experimented by inductively coupled plasma emission spectrometer Agilent ICP-OES 730-ES, USA. The Py-IR test was performed using a Thermo-Nicolet IS10 instrument.

2. $Pd_{1.4}Fe_1/TiO_{2-x}$ Preparation Method

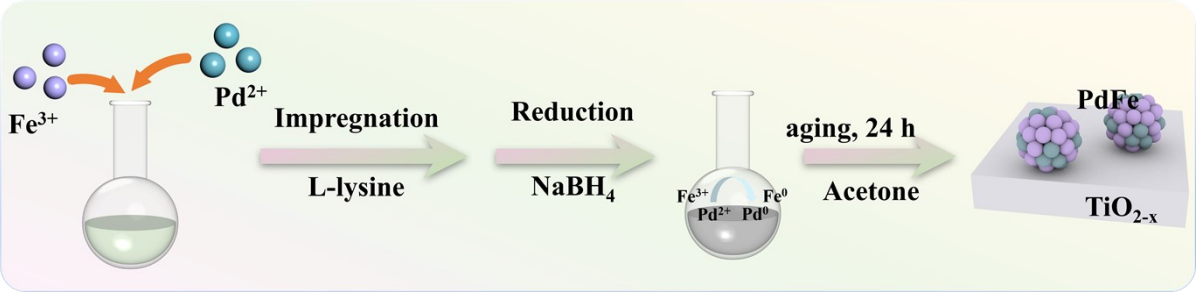

Figure S1. Schematic representation of the preparation process of $Pd_{1.4}Fe_1/TiO_{2-x}$.

3. ICP results test

Table S1. ICP results.

Entry	Catalysts	Theoretical Pd:Fe ratio	Actual Pd:Fe ratio
1	Pd_1Fe_1/TiO_{2-x}	1:1	0.87:1
2	$Pd_{1.4}Fe_1/TiO_{2-x}$	1.4:1	1.31:1
3	Pd_2Fe_1/TiO_{2-x}	2:1	1.66:1

4. Physical properties of catalysts

Table S2. Physical properties of supported catalysts.

Catalyst.	BET surface area/m^2 g-cat^{-1}	t-Plot micropore volume/ m^3 g-cat^{-1}	Averagepore diameter/nm
TiO_2	263.4	0.12	5.6
Pd/TiO_{2-x}	221.3	0.07	6.6
Fe/TiO_{2-x}	247.5	0.10	6.0
$Pd_{1.4}Fe_1/TiO_{2-x}$	206.6	0.09	6.2

5. Screening of direct HDO reaction conditions

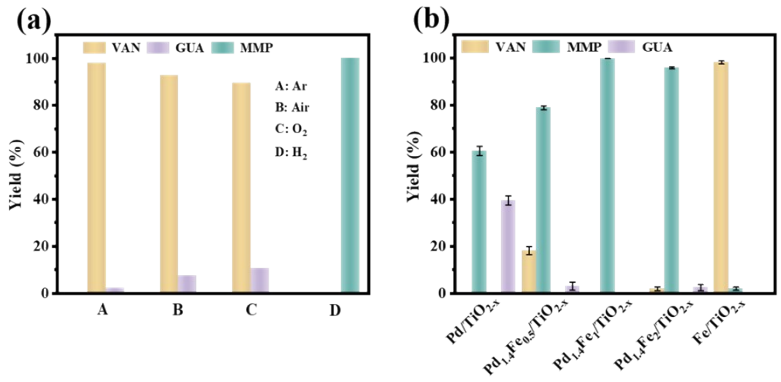

Figure S2. (a) Screening of reaction atmospheres for vanillin HDO reaction. (b) Direct HDO performance of bimetallic catalysts with different proportions.

6. Characterization data

Table S3. Binding energies and atomic ratios of catalysts obtained from XPS.

Catalysts	Binding Energy (eV)							
	Pd^0 $3d_{5/2}$	Pd^{2+} $3d_{5/2}$	Pd^0 $3d_{3/2}$	Pd^{2+} $3d_{3/2}$	Fe^{2+} $2p_{3/2}$	Fe^{3+} $2p_{3/2}$	Fe^{2+} $2p_{1/2}$	Fe^{3+} $2p_{1/2}$
Pd/TiO_{2-x}	335.1	336.7	340.5	342.3	/	/	/	/
Fe/TiO_{2-x}	/	/	/	/	709.9	714.0	722.6	726.1
$Pd_{1.4}Fe_1/TiO_{2-x}$	334.7	335.7	339.9	341.6	709.3	714.0	722.5	726.9

Sample Preparation Method:

The study employed photoelectrochemical testing to investigate the correlations between the exposed crystal plane of the catalyst and three key electrochemical properties: photocurrent density, charge carrier conductivity, and the flat-band potential position. The aforementioned tests were conducted using a standard three-electrode system. Platinum foil served as the counter electrode, Ag/AgCl (in saturated potassium chloride solution) as the reference electrode, and fluorinated tin oxide (FTO) glass uniformly coated with the catalyst as the working electrode. The working electrode was prepared as follows: FTO glass (1 cm×2 cm) was ultrasonicated in ethanol and water for 20 min each to remove surface impurities, and then dried in a vacuum oven at 80 °C. Subsequently, 4 mg of catalyst was dispersed in a mixed solution of 320 μL deionized water and 160 μL anhydrous ethanol, followed by ultrasonication for 5 min to prepare the catalyst ink. Subsequently, 20 μL of Nafion solution was added dropwise, followed by ultrasonication for 3 h to disperse the catalyst uniformly with Nafion. The cleaned FTO conductive glass was then placed on a heating plate at 80°C, and the ink solution was gradually applied in multiple steps over a 1 cm×1 cm area to coat the electrode. Finally, the coated electrode was dried in a vacuum oven at 80°C for 12 h. Photoelectrochemical testing was conducted in a 0.5 $mol \cdot L^{-1}$ Na_2SO_4 aqueous solution. Prior to measurement, the solution was purged with N_2 for 30 min to remove dissolved oxygen.

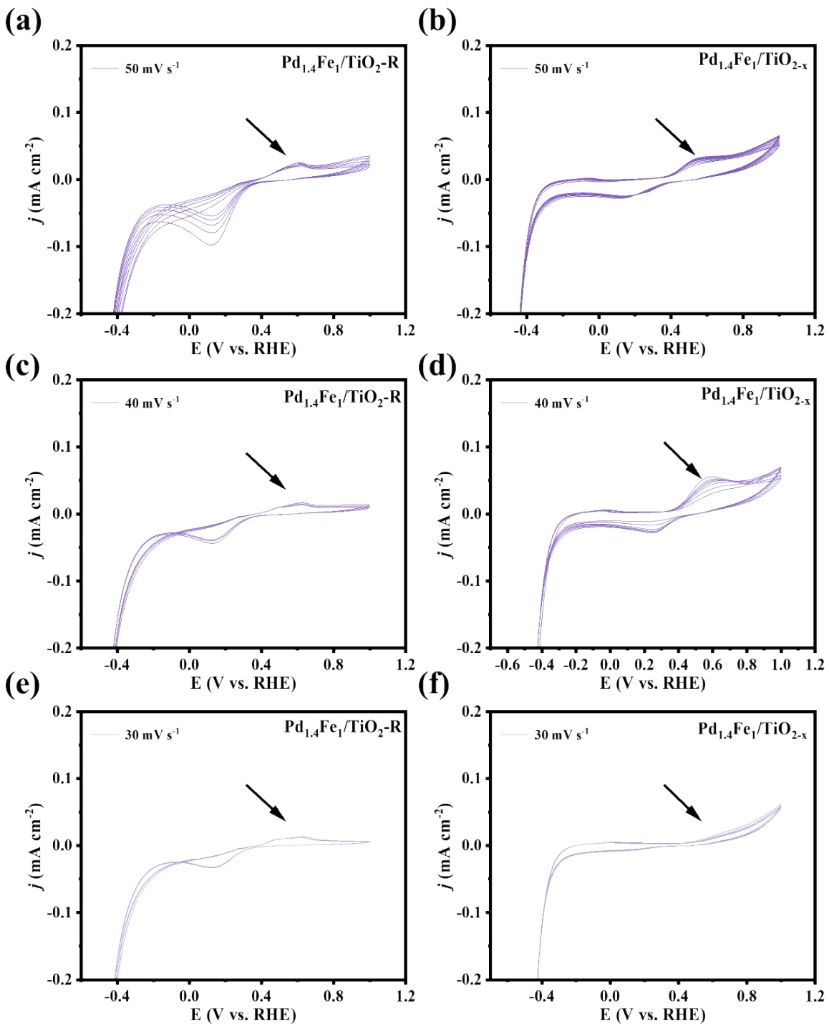

Figure S4. The yield of VAN direct HDO at 140 °C for $Pd_{1.4}Fe_1$ NPs on different supports. CV curves of $Pd_{1.4}Fe_1/TiO_2$-R and $Pd_{1.4}Fe_1/TiO_{2-x}$ with the different scan rate in Ar-saturated 0.5 M H_2SO_4.

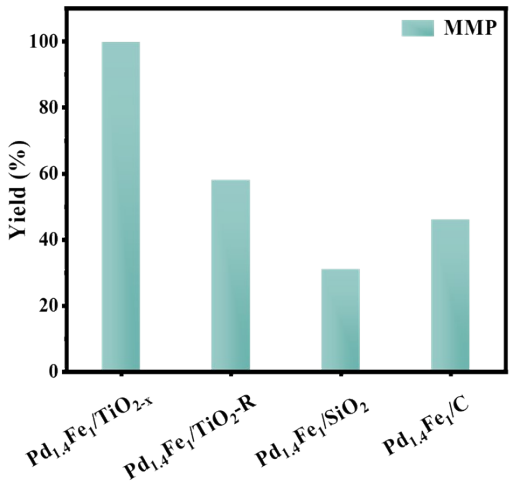

Figure S5. The yield of VAN direct HDO at 140 °C for $Pd_{1.4}Fe_1$ NPs on different supports.

7. Overview of vanillin HDO

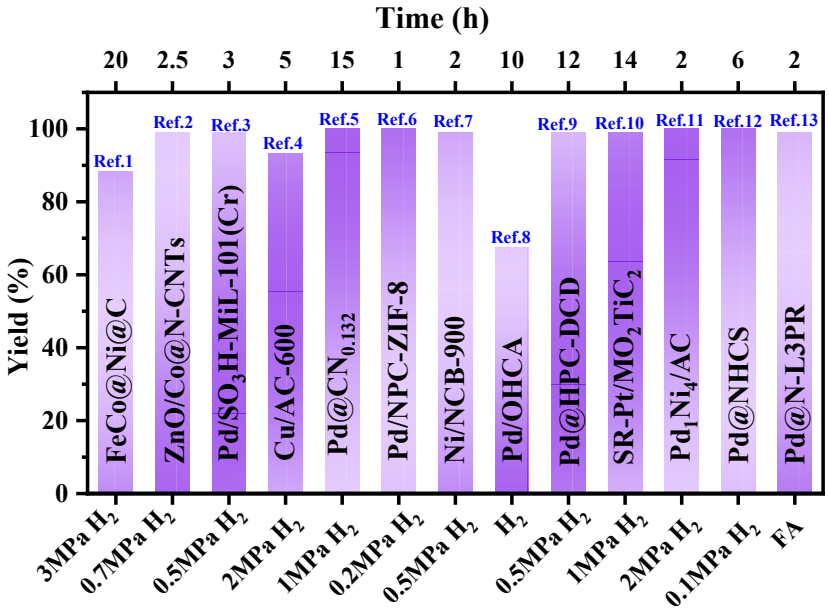

Figure S3. Aqueous phase HDO reaction.

Table S4. Summary of different heterogeneous catalysts for the HDO reaction of VAN in recent published works.

Catalyst	Hydrogen donor	Temperature/°C	Time/h	Solvent	Yield	Ref.
$Pd_{1.4}Fe_1/TiO_{2-x}$	**0.1 MPa H_2**	**140**	**3**	**none**	**99%**	***This work***
Pd/C	H_2	55	24	Acetic acid	**70%**	***14***
Au/Co_3O_4 NRs-OVs	0.1 MPa N_2	240	3	IPA	93%	15
Pd/PAF-30	1 MPa N_2	80	2	IPA	99%	*16*
$Pd/CuFe_2O_4$	N_2	150	2	IPA	99%	*17*
Co/CN-0.5-750	0.5 MPa N_2	180	2	IPA	97%	*18*
ZrO_2-1	5 MPa H_2	180	24	IPA	92%	*19*
Cu/DMSN	0.5 MPa H_2	240	3	EtOH	99%	*20*
Cu/MgO	4 MPa H_2	160	4	EtOH	99%	*21*
Pd/Nb_2O_5	PMHS	RT	0.5	EtOH	99%	*22*
Pd/ZrO_2	PMHS	35	1	n-butanol	99%	*23*

Co@NC-SBA	1 MPa H_2	140	3	H_2O-MeOH	93%	*24*
NiZnAl-MMO/ZrO_2	1 MPa H_2	130	2	H_2O-MeOH	98%	*25*
PdAu/g-C_3N_4	88wt% FA	RT	1	H_2O-ethanol	99%	*26*
Pd/NC-BT	1 MPa H_2	25	3.5	THF	91%	*27*
Pd/C-CaH_2	/	100	20	THF	96%	*28*
$NH_3 \cdot BH_3$ $TiCl_4$	/	RT	1	DCM	76%	*29*
CuO/Al_2O_3	0.5 MPa N_2	120	8	Diox	84%	*30*
Ni_2-WO_x@CN	2 MPa H_2	140	2.5	ethanol	100%	*31*
$CoRe_{0.1}/TiO_2$	2 MPa H_2	180	2	IPA	67.4%	*32*
$NiRe_{0.15}$/MCSs	2 MPa H_2	150	4	ethanol	99%	*33*

References

(1) C. Cerezo-Navarrete, I. M. Marin, H. García-Miquel, A. Corma, B. Chaudret and L. M. Martinez-Prieto, Magnetically induced catalytic reduction of biomass-derived oxygenated compounds in water, *ACS Catal.*, 2022, **12**, 8462−8475.

(2) V. Ranaware, D. Verma, R. Insyani, A. Riaz, S. M. Kim and J. Kim, Highly-efficient and magnetically-separable ZnO/Co@N-CNTs catalyst for hydrodeoxygenation of lignin and its derived species under mild conditions, *Green Chem.*, 2019, **21**, 1021−1042.

(3) F. M. Zhang, Y. Jin, Y. H. Fu, Y. J. Zhong, W. D. Zhu, A. A. Ibrahim and M. S. El-Shall, Palladium nanoparticles incorporated within sulfonic acid-functionalized MIL-101(Cr) for efficient catalytic conversion of vanillin, *J. Mater. Chem. A*, 2015, **3**, 17008−17015.

(4) R. Y. Fan, C. Chen, M. M. Han, W. B. Gong, H. M. Zhang, Y. X. Zhang, H. J. Zhao and G. Z. Wang, Highly dispersed copper nanoparticles supported on activated carbon as an efficient catalyst for selective reduction of vanillin, *Small*, 2018, **14**, 1801953.

(5) X. Xu, Y. Li, Y. T. Gong, P. F Zhang, H. R Li and Y. Wang, Synthesis of palladium nanoparticles supported on mesoporous N-doped carbon and their catalytic ability for biofuel upgrade, *J. Am. Chem. Soc.*, 2012, **134**, 16987−16990.

(6) Y. Z. Chen, G. R. Cai, Y. M. Wang, Q. Xu, S. H. Yu and H. L. Jiang, Palladium nanoparticles stabilized with N-doped porous carbons derived from metal-organic frameworks for selective catalysis in biofuel upgrade: the role of catalyst wettability, *Green Chem.*, 2016, **18**, 1212−1217.

(7) R. F. Nie, H. H. Yang, H. F. Zhang, X. L. Yu, X. H. Lu, D. Zhou and Q. H. Xia, Mild-temperature hydrodeoxygenation of vanillin over porous nitrogen-doped carbon black supported nickel nanoparticles, *Green Chem.*, 2017, **19**, 3126−3134.

(8) J. S. Ran, R. X. YangCheng, Y. T. Cui and J. J. Wang, Promotion of sulfonic acid groups on biomass carbons loading ultrafine palladium nanoparticles for the efficient hydrodeoxygenation of vanillin in water, *Curr. Res. Green Sustain. Chem.*, 2022, **5**, 100230.

(9) C. Pu, J. Zhang, G. Chang, Y. Y. Xiao, X. C. Ma, J. Wu, T. T. Lou, K. X. Huang, S. C. Ke, J. X. Li and X. Y. Yang, Nitrogen precursor-mediated construction of N-doped

hierarchically porous carbon-supported Pd catalysts with controllable morphology and composition, *Carbon*, 2020, **159**, 451−460.

(10) Z. J. Zhao, S. T. Huang, G. L. Dong, Y. Chen, M. X. Wang, M. L. Xia, X. Song, X. N. Li, Z. Z. Wei and J. W. Wang, Engineering the electronic structure of Pt for selective hydrogenation of vanillin to vanillyl alcohol and p-cresol, *Chem. Eng. Sci.*, 2024, **300**, 120616.

(11) J. W. Zhang, K. K. Sun, D. D. Li, T. Deng, G. P. Lu and C. Cai, Pd-Ni bimetallic nanoparticles supported on active carbon as an efficient catalyst for hydrodeoxygenation of aldehydes, *Appl. Catal. A*, 2019, **569**, 190−195.

(12) J. Wu, L. Q. Liu, X. Y. Yan, G. Pan, J. H. Bai, C. B. Wang, F. W. Li and Y. Li, Microenvironment engineering of nitrogen-doped hollow carbon spheres encapsulated with Pd catalysts for highly selective hydrodeoxygenation of biomass-derived vanillin in water, *Chin. J. Catal.*, 2025, **71**, 267−284.

(13) T. R. Pang, Z. L. Xue, G. H. Wang, J. K. Li, W. J. Sui and C. L. Si, Non-carbonized Pd single-atom catalyst supported on lignin-functionalized phenolic resin for potent catalytic transfer hydrogenation of lignin-derived aldehydes, *Angew. Chem. Int. Ed.*, 2025, **64**, e202503195.

(14) Q. Wang, Y. Yang, Y. Li, W. Yu and Z. J. Hou, An efficient method for the synthesis of lignans, *Tetrahedron*, 2006, **62**, 6107−6112.

(15) Q. L. Liao, M. Shi, Q. X. Zhang, W. H. Cheng, P. Y. Ji, X. L. Fu, H. R. Lai, R. Z. Fan, J. Sheng and H. Li, Gold catalyst anchored to pre-reduced Co_3O_4 nanorods for the hydrodeoxygenation of vanillin using alcohols as hydrogen donors, *ACS Appl. Mater. Interfaces*, 2022, **14**, 3939−3948.

(16) M. A. Bazhenova, L. A. Kulikov, Y. S. Bolnykh, A. L. Maksimov and E. A. Karakhanov, Palladium catalysts based on porous aromatic frameworks for vanillin hydrogenation: tuning the activity and selectivity by introducing functional groups, *Catal. Commun.*, 2022, **170**, 106486.

(17) G. S. More, D. R. Kanchan, A. Banerjee and R. Srivastava, Selective catalytic

hydrodeoxygenation of vanillin to 2-methoxy-4-methyl phenol and 4-methyl cyclohexanol over Pd/$CuFe_2O_4$ and PdNi/$CuFe_2O_4$ catalysts, *Chem. Eng. J.*, 2023, **462**, 142110.

(18) X. Wu, H. Li, F. Ge, W. L. Xu, H. L. Lu, M. H. Zhou, N-doped MOF-lignin hybrid catalyst for highly selective hydrodeoxygenation of lignin-derived phenols, *Chem. Eng. J.*, 2024, **495**, 153009.

(19) X. M. Wang, Y. Zhang, J. Z. Chen and Y. S. Xu, Mesoporous zirconium oxides and cobalt oxides for selective hydrodeoxygenation of vanillin, *Catal. Lett.*, 2024, **154**, 3195−3211.

(20) C. H. Wang, M. Y. Wang, L. Chen, N. Z. Shang, W. Gao, X. Cheng, S. T. Gao, Y. J. Gao and C. Wang, Construction of dendritic mesoporous SiO_2 supported Cu catalyst for hydrodeoxidation of lignin derivatives, *Bioresour. Technol.*, 2024, **413**, 131503.

(21) K. Sun, Y. W. Shao, C. Ming, M. J. Fan, H. L. Fan, L. J. Zhang, S. Zhang, Y. Zhang, G. Z. Chen and X. Hu, Copper-based catalysts synthesized during hydrogenation, *Chem. Eng. Sci.*, 2023, **276**, 118819.

(22) H. Xu and H. Li, Regulating the crystal phase of Pd/Nb_2O_5 for vanillin selective HDO at room temperature, *J. Catal.*, 2023, **423**, 105−117.

(23) X. Zhang, J. Y. Jiang and H. Li, Critical role of support crystal structures on highly selective hydrodeoxygenation of lignin-derived vanillin over Pd/ZrO_2 catalysts, *Fuel Process. Technol.*, 2023, **249**, 107844.

(24) L. K. Zhang, N. Z. Shang, S. T. Gao, J. M. Wang, T. Meng, C. C. Du, T. D. Shen, J. Y. Haung, Q. H. Wu, Y. Q. Qiao, C. Wang, Y. J. Gao and Z. Wang, Atomically dispersed Co catalyst for efficient hydrodeoxygenation of lignin-derived species and hydrogenation of nitroaromatics, *ACS Catal.*, 2020, **10**, 8672−8682.

(25) X. K. Yue, L. H. Zhang, L. X. Sun, S. T. Gao, W. Gao, X. Cheng, N. Z. Shang, Y. J. Gao and C. Wang, Highly efficient hydrodeoxygenation of lignin-derivatives over Ni-based catalyst, *Appl. Catal. B*, 2021, **293**, 120243.

(26) P. Y. Wu, D. X Zhao, G. P. Lu and C. Cai, Supported Pd-Au bimetallic nanoparticles as an efficient catalyst for the hydrodeoxygenation of vanillin with formic acid at room temperature, *Green Chem.*, 2022, **24**, 1096−1102.

(27) S. G. Wang, P. Zhou, L. Jiang, Z. H. Zhang, K. J. Deng, Y. H. Zhang, Y. X. Zhao, J. L. Li, S. Bottle and H. Y. Zhu, Selective deoxygenation of carbonyl groups at room temperature and atmospheric hydrogen pressure over nitrogen-doped carbon supported Pd catalyst, *J. Catal.*, 2018, **368**, 207−216.

(28) N. Lezana-Tobar, R. López and R. Robles-Henríquez, Hydrodeoxygenation of carbonyl compounds biomass derivatives using CaH_2 over Pd/C, *Chem. Select*, 2024, **9**, e202304105.

(29) Y. J. Zang, Y. F. Ma, Q. L. Xu, N. D. Chen, X. Li and F. C. Zhu, $TiCl_4$-mediated deoxygenative reduction of aromatic ketones to alkylarenes with ammonia borane, *Org. Biomol. Chem.*, 2024, **22**, 932−939.

(30) D. Y. Guo, S. Wang, S. L. Dong, J. F. Feng and H. Pan, Hydrodeoxygenation of vanillin to 2-methoxy-4-methylphenol over in-situ reduced CuO/Al_2O_3 catalysts under mild conditions, *Chem. Eng. J.*, 2024, **487**, 150428.

(31) L. G. Ma, G. Y. Zhang, S. X. Dou, Y. Y. Dong and X. J. Kong, WO_x boosted hollow Ni nanoreactors for the hydrodeoxygenation of lignin derivatives, *Int. J. Biol. Macromol.*, 2024, **269**, 132156.

(32) Z. F. Hu, Q. Chen, J. J. Jia and X. J. Kong, Highly dispersed Co–Re bimetallic catalyst for lignin derivative upgrading: Oxygen vacancy engineering and mechanistic insights, *Chem. Eng. J.*, 2025, **522**, 167155.

(33) L. G. Ma, G. Y. Zhang, Y. Y. Dong, S. X. Dou, Q. Meng, P. J. Yan, L. Y. Liu and X. J. Kong, Hydrodeoxygenation of lignin derivatives over Ni-Re bimetallic catalyst supported on mesoporous carbon sphere, *J. Environ. Chem. Eng.*, 2023, **11**, 110215.

8. Recyclability test

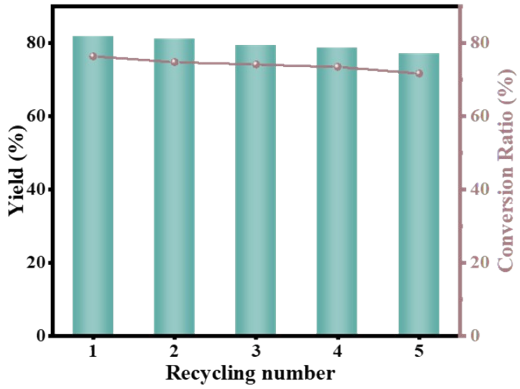

Figure S6. Cyclic stability test under low conversion ratio.

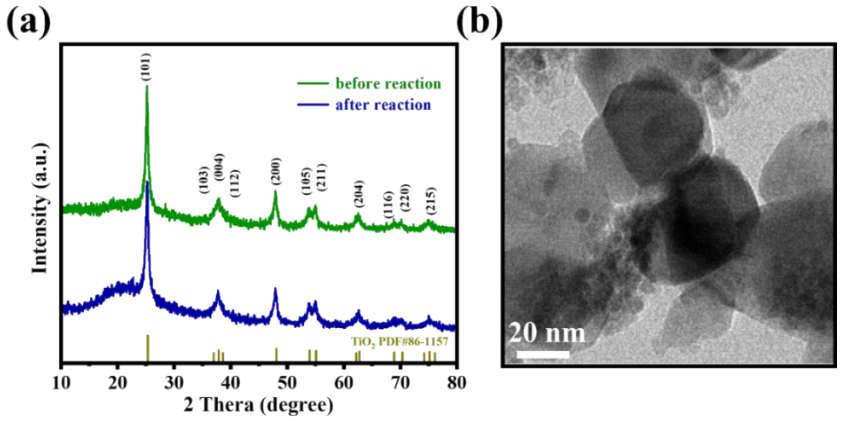

Figure S7. (a) XRD and (b) TEM images of the $Pd_{1.4}Fe_1/TiO_{2-x}$ catalyst after five recycling cycles.

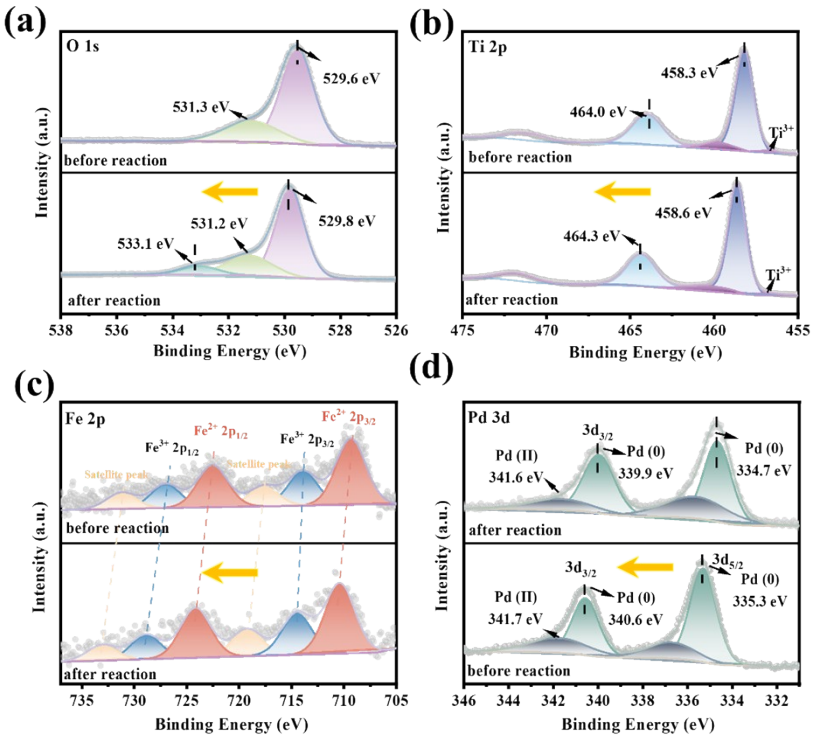

Figure S8. XPS comparison of $Pd_{1.4}Fe_1/TiO_2$ catalyst before and after cycles, (a) O 1s, (b) Ti 2p, (c) Fe 2p, (d) Pd 3d.

9. GC chromatogram of the compounds

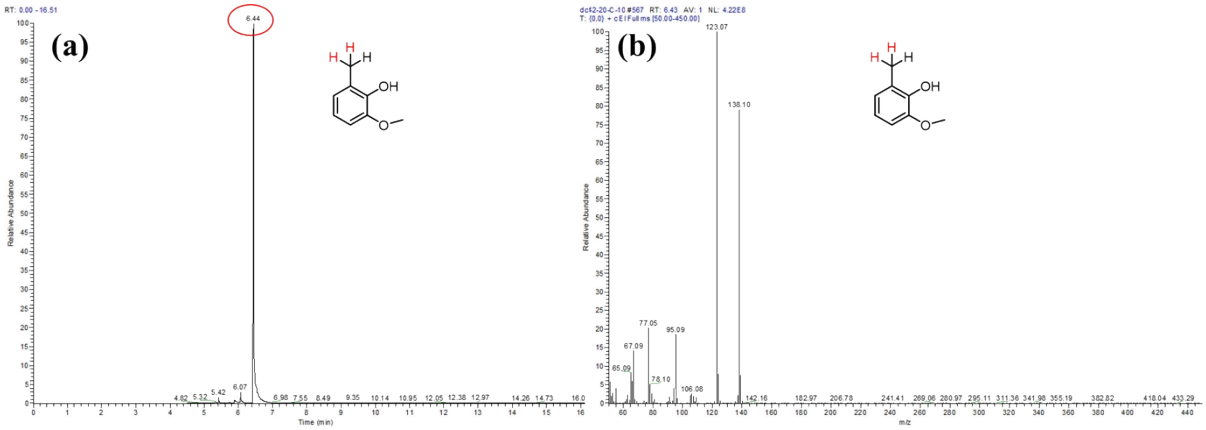

The (a) GC chromatograms and (b) Mass spectrum of **2b.**

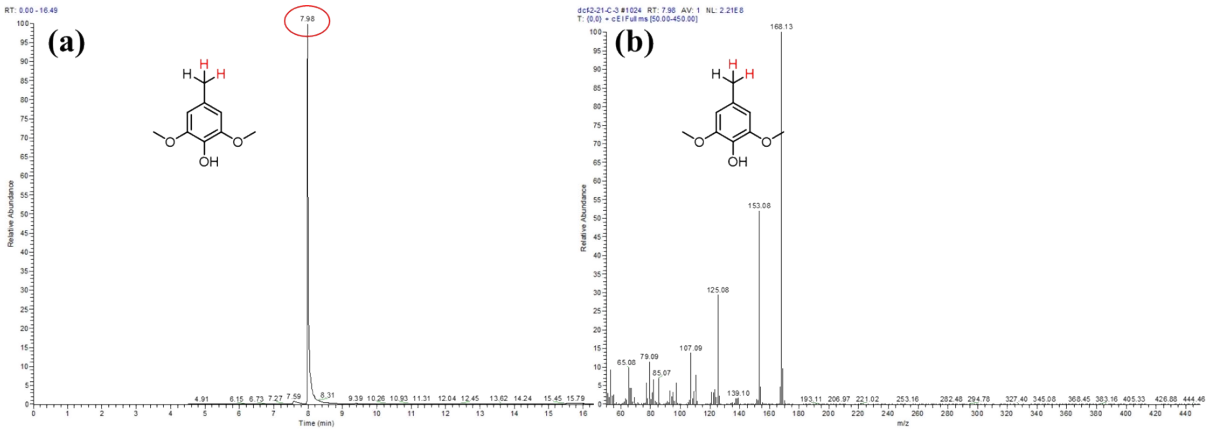

The (a) GC chromatograms and (b) Mass spectrum of **2c.**

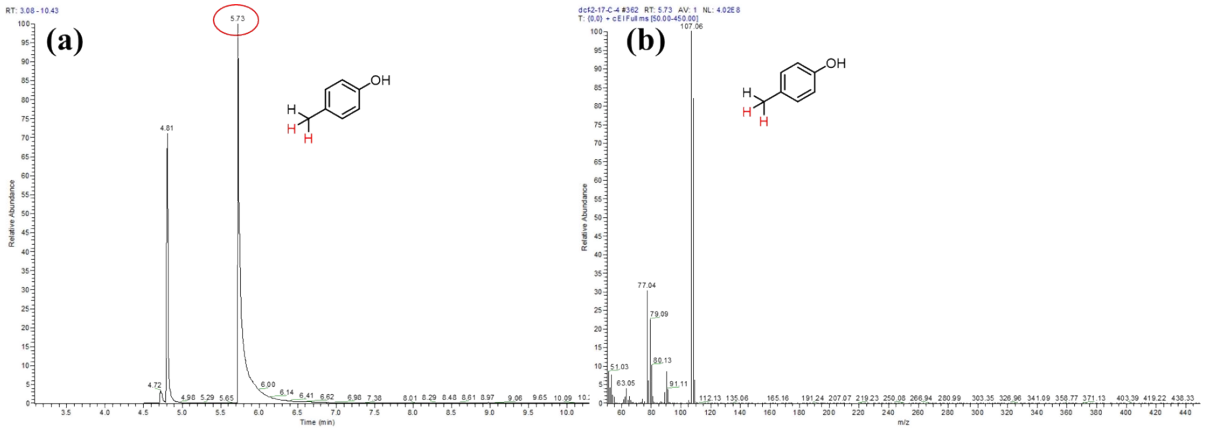

The (a) GC chromatograms and (b) Mass spectrum of **2e.**

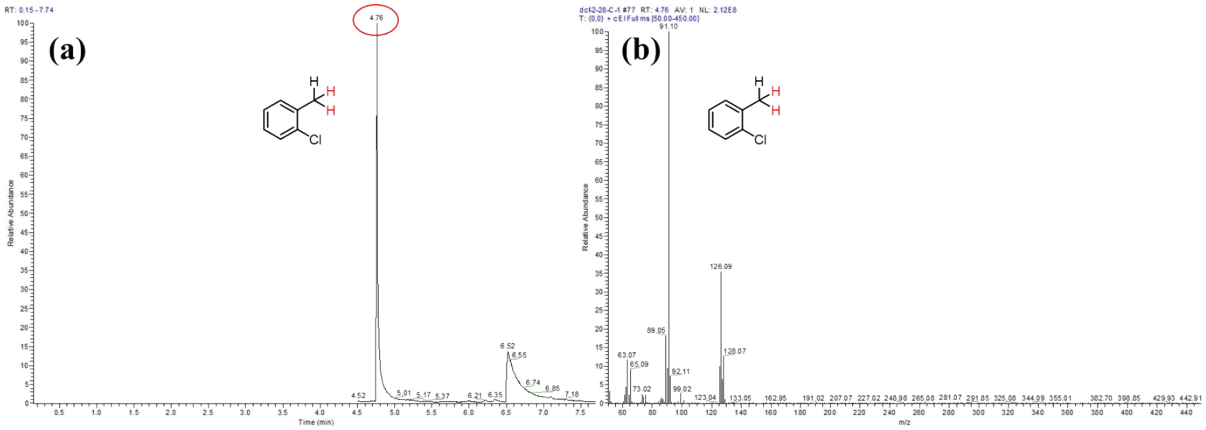

The (a) GC chromatograms and (b) Mass spectrum of **2g.**

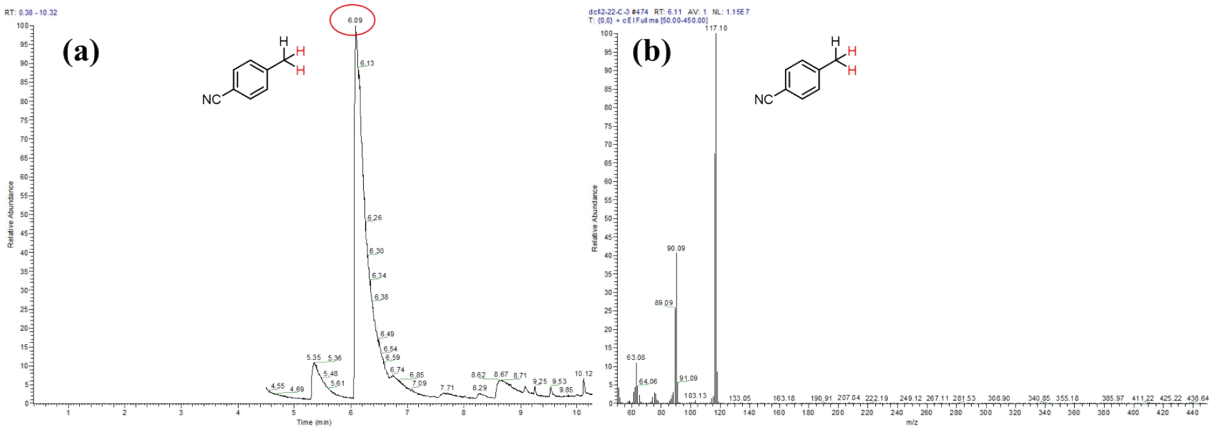

The (a) GC chromatograms and (b) Mass spectrum of **2l.**

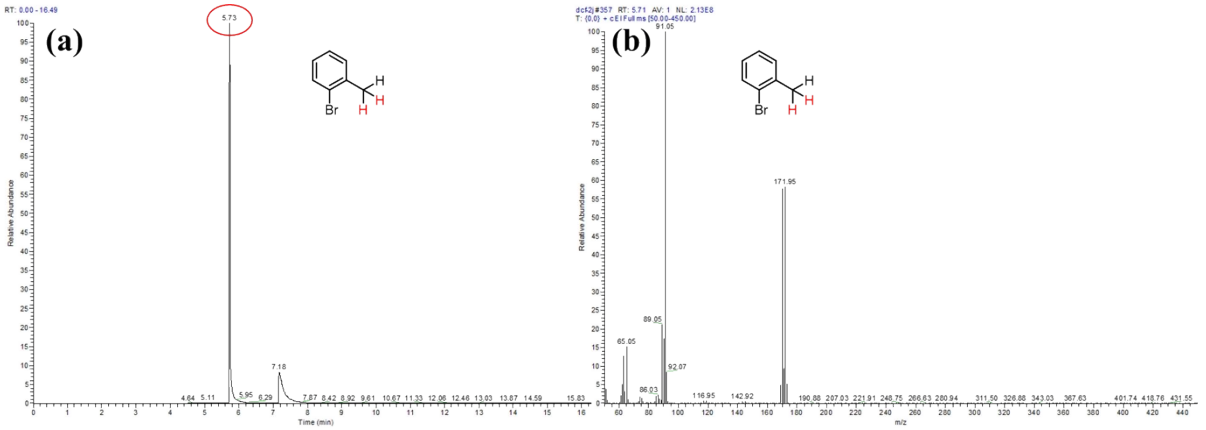

The (a) GC chromatograms and (b) Mass spectrum of **2j.**

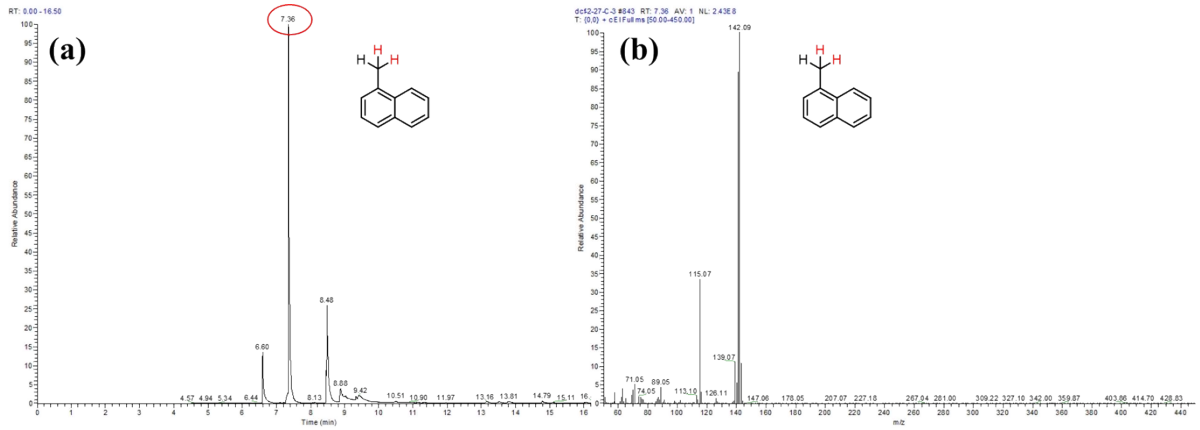

The (a) GC chromatograms and (b) Mass spectrum of **2m.**

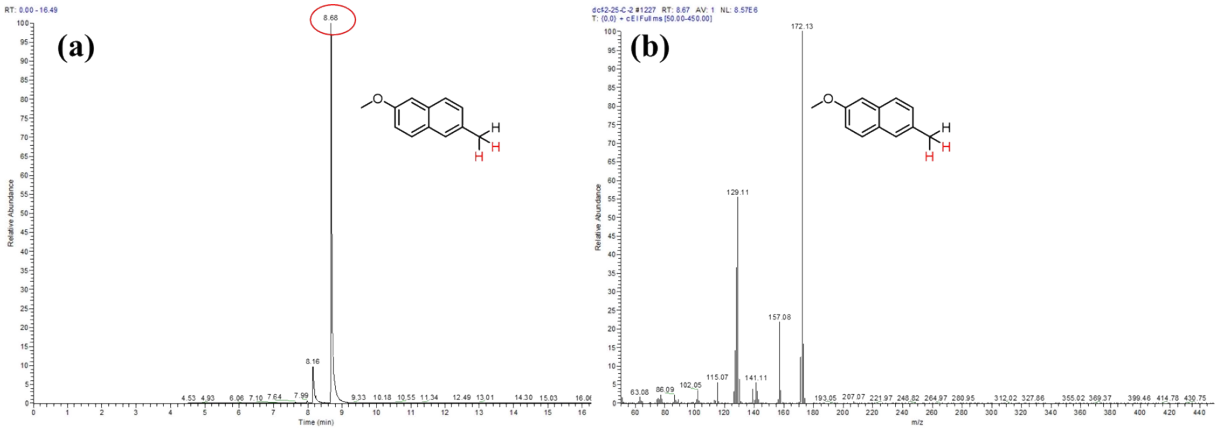

The (a) GC chromatograms and (b) Mass spectrum of **2o.**

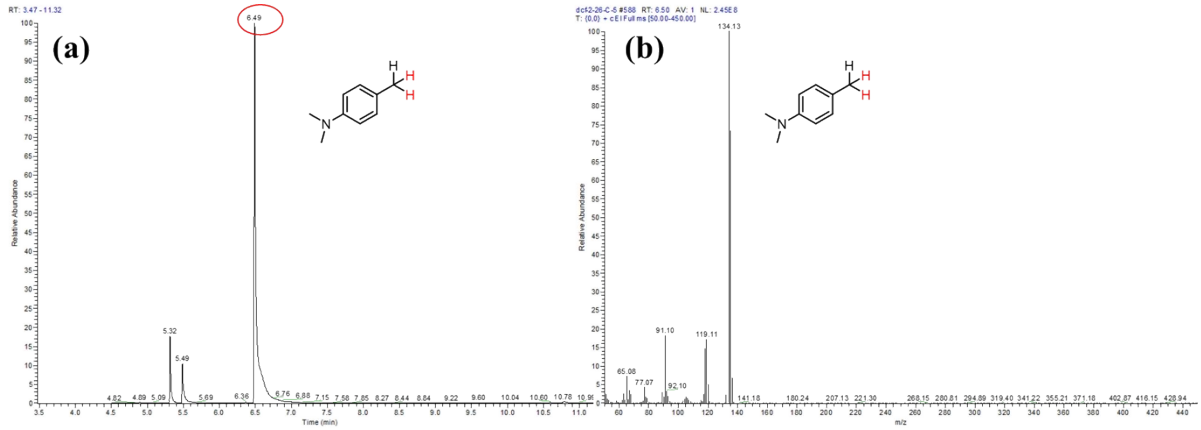

The (a) GC chromatograms and (b) Mass spectrum of **2q.**

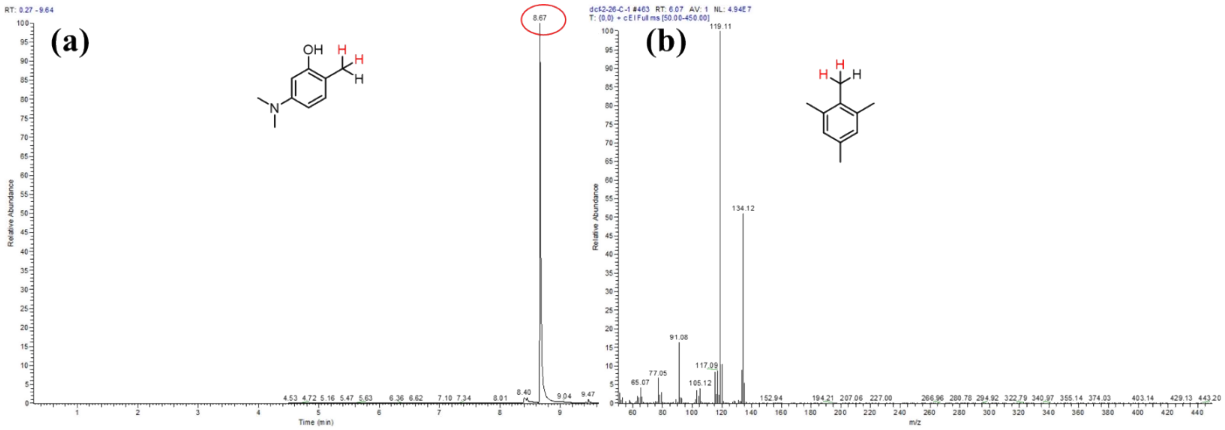

The (a) GC chromatograms of **2r** and (b) Mass spectrum of **2s.**

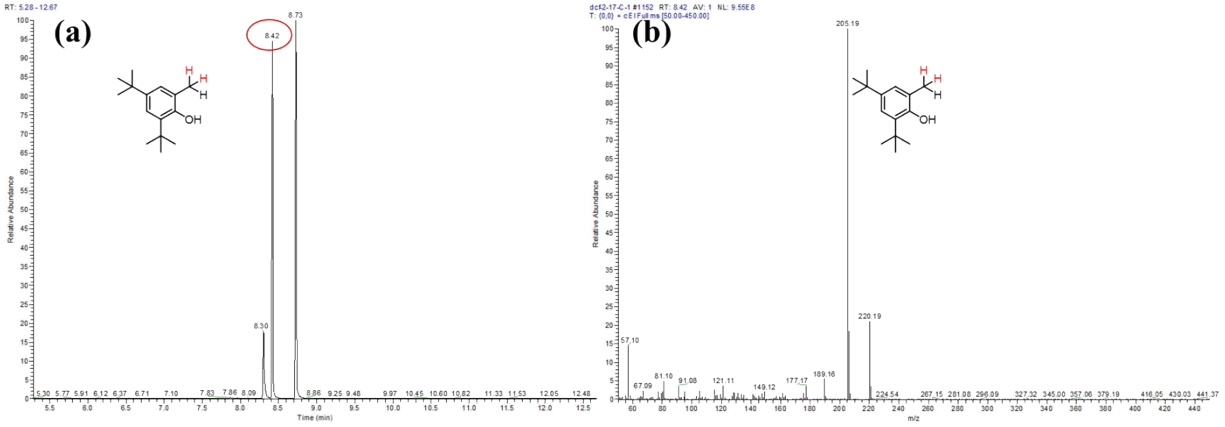

The (a) GC chromatograms and (b) Mass spectrum of **2t.**

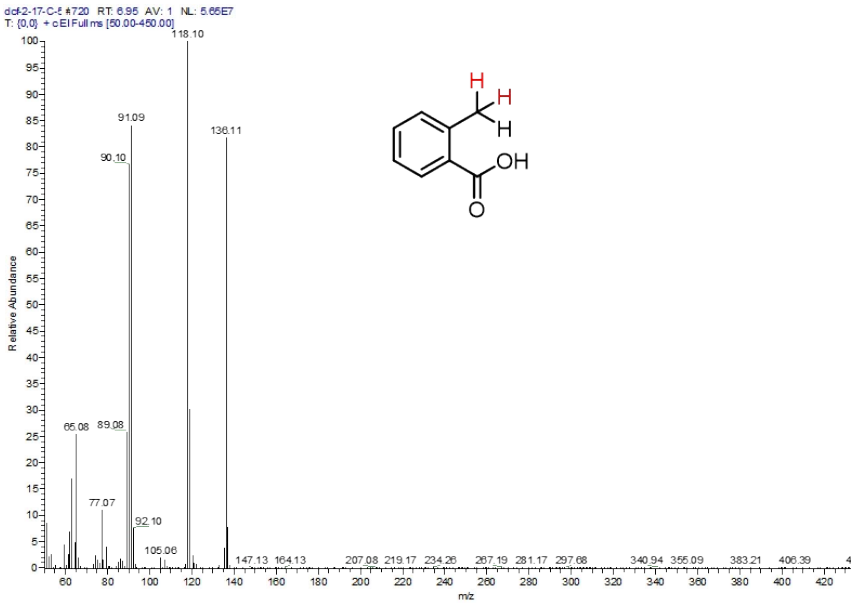

The Mass spectrum of **2u.**

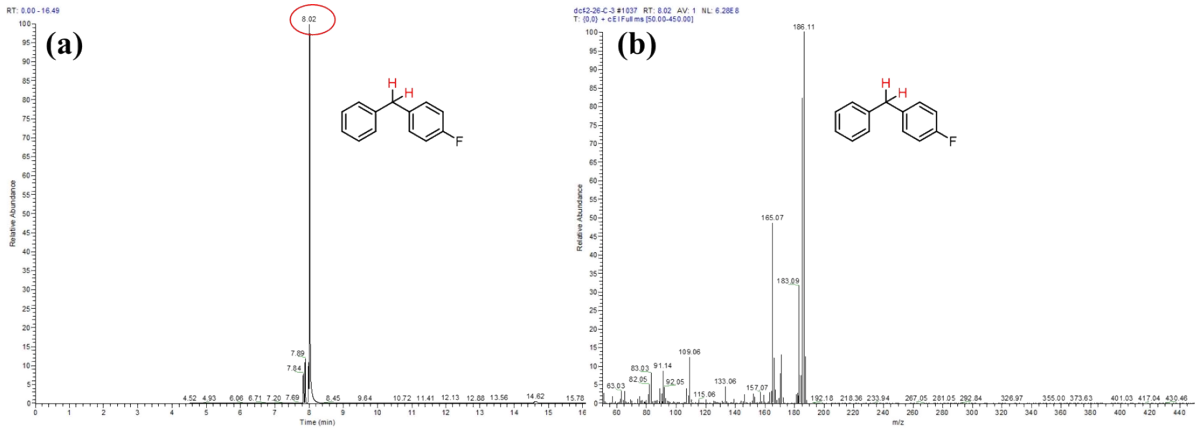

The (a) GC chromatograms and (b) Mass spectrum of **4b.**

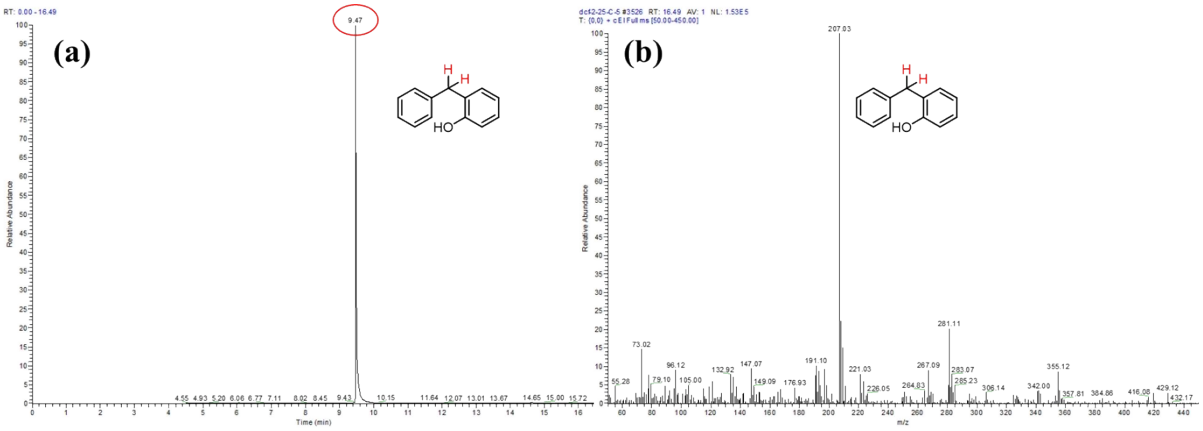

The (a) GC chromatograms and (b) Mass spectrum of **4c.**

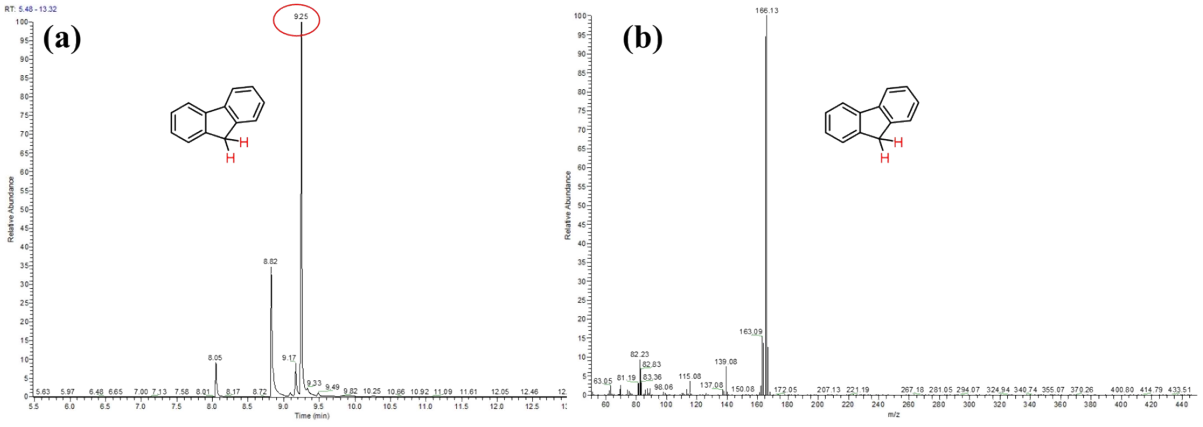

The (a) GC chromatograms and (b) Mass spectrum of **4d.**

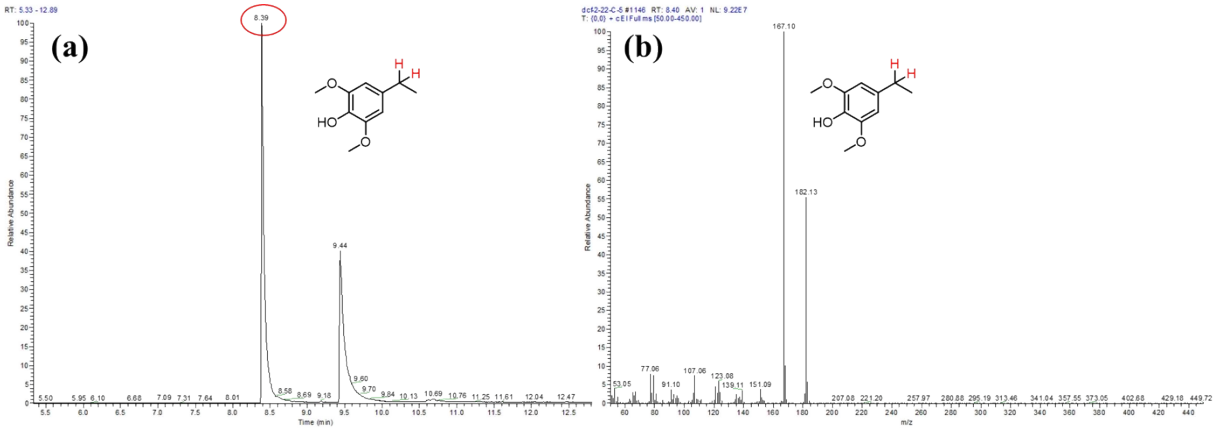

The (a) GC chromatograms and (b) Mass spectrum of **4f.**

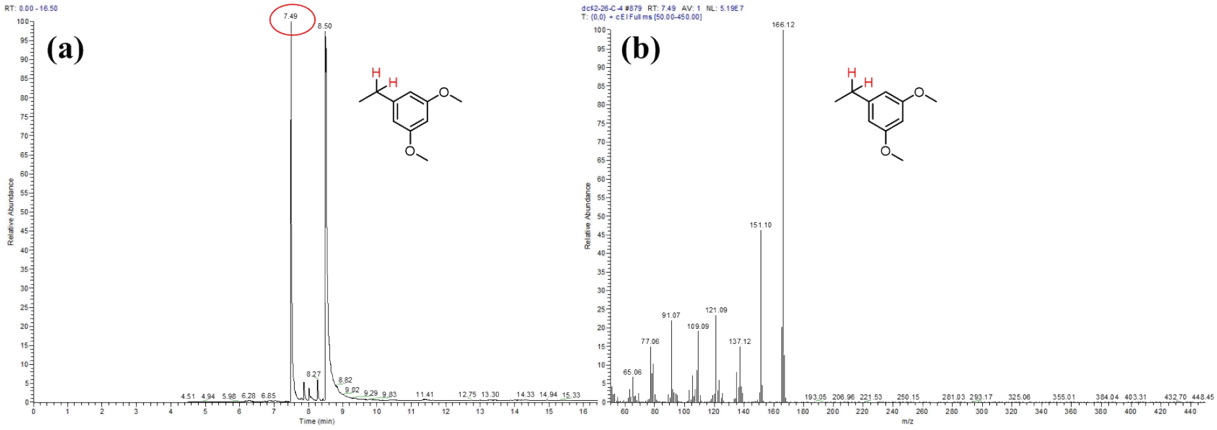

The (a) GC chromatograms and (b) Mass spectrum of **4g.**

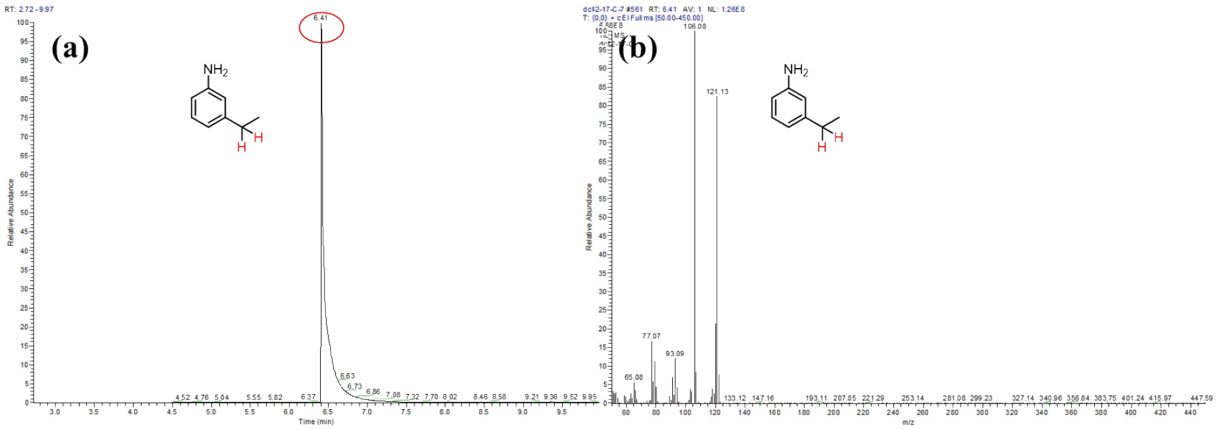

The (a) GC chromatograms and (b) Mass spectrum of **4h.**

10. Procedure for purification of products from the reaction mixture

Catalyst separation: Upon completion of the reaction, the mixture was cooled to room temperature and centrifuged at 9000 rpm for 2 min to separate the solid $Pd_{1.4}Fe_1/TiO_{2-x}$ catalyst from the supernatant. The catalyst was collected for direct reuse in subsequent cycles, while the supernatant was subjected to further purification

Compound **2a** is a colorless liquid ($C_8H_{10}O_2$). The crude product showed an R*f* value of approximately 0.57 on TLC (PE/EA=9:1, v/v) when visualized under UV light at 254 nm. Purification was performed by silica gel column chromatography (200-300 mesh) using an isocratic eluent system of PE/EA (10:1, v/v) to afford the pure target compound.

Compound **2b** is a white solid ($C_8H_{10}O_2$). The crude product showed an R*f* value of approximately 0.51 on TLC (PE/EA=9:1, v/v) when visualized under UV light at 254 nm. Purification was performed by silica gel column chromatography (200-300 mesh) using an isocratic eluent system of PE/EA (10:1, v/v) to afford the pure target compound.

Compound **2c** is a colorless transparent liquid ($C_9H_{12}O_3$). TLC was conducted with PE/EA (7:3, v/v) as the developing solvent, visualized under a 254 nm UV lamp, and the R*f* was approximately 0.45. The crude product was purified by preparative TLC and eluted with EA, ultimately yielding the target compound in pure form.

Compound **2d** is a colorless transparent liquid ($C_8H_{10}O$). TLC was conducted with PE/EA (8:2, v/v) as the developing solvent, visualized under a 254 nm UV lamp, and the R*f* was approximately 0.40. The crude product was purified by preparative TLC and eluted with EA, ultimately yielding the target compound in pure form.

Compound **2e** is colorless liquid (C_7H_8O). The crude product showed an R*f* value of approximately 0.37 on TLC (PE/EA=9:1, v/v) when visualized under UV light at 254 nm. Purification was performed by silica gel column chromatography (200-300 mesh) using a gradient eluent system of PE/EA (15:1-9:1, v/v) to afford the pure target compound.

Compound **2g** is a transparent liquid (C_7H_7Cl). TLC was conducted with PE/EA (9:1, v/v) as the developing solvent, visualized under a 254 nm UV lamp, and the R*f* was approximately

0.43. The crude product was purified by preparative TLC and eluted with EA, ultimately yielding the target compound in pure form.

Compound **2h** is a transparent liquid (C_7H_7Cl). TLC was conducted with PE/EA (9:1, v/v) as the developing solvent, visualized under a 254 nm UV lamp, and the R*f* was approximately 0.45. The crude product was purified by preparative TLC and eluted with EA, ultimately yielding the target compound in pure form.

Compound **2l** is white solid (C_8H_7N). The crude product showed an R*f* value of approximately 0.5. on TLC (PE/EA=6:4, v/v) when visualized under UV light at 254 nm. Purification was performed by silica gel column chromatography (200-300 mesh) using a gradient eluent system of PE/EA (10:1-1:1, v/v) to afford the pure target compound.

Compound **2m** is a colorless liquid ($C_{11}H_{10}$). TLC was conducted with PE as the developing solvent, visualized under a 254 nm UV lamp, and the R*f* was approximately 0.46. The crude product was purified by preparative TLC and eluted with EA, ultimately yielding the target compound in pure form.

Compound **2o** is a colorless liquid ($C_{12}H_{12}O$). TLC was conducted with PE/EA (9:1, v/v) as the developing solvent, visualized under a 254 nm UV lamp, and the R*f* was approximately 0.54. The crude product was purified by preparative TLC and eluted with EA, ultimately yielding the target compound in pure form.

Compound **2q** is a yellow liquid ($C_9H_{13}N$). TLC was conducted with PE/EA (10:1, v/v) as the developing solvent, visualized under a 254 nm UV lamp, and the R*f* was approximately 0.50. The crude product was purified by preparative TLC and eluted with EA, ultimately yielding the target compound in pure form.

Compound **4a** is a yellow liquid ($C_{13}H_{12}$). TLC was conducted with PE as the developing solvent, visualized under a 254 nm UV lamp, and the R*f* was approximately 0.38. The crude product was purified by preparative TLC and eluted with PE, ultimately yielding the target compound in pure form.

Compound **4b** is a colorless liquid ($C_{13}H_{11}F$). TLC was conducted with PE as the developing solvent, visualized under a 254 nm UV lamp, and the R*f* was approximately 0.41. The crude

product was purified by preparative TLC and eluted with EA, ultimately yielding the target compound in pure form.

Compound **4d** is a white solid ($C_{13}H_{10}$). TLC was conducted with PE/EA (8:2, v/v) as the developing solvent, visualized under a 254 nm UV lamp, and the R*f* was approximately 0.47. The crude product was purified by preparative TLC and eluted with EA, ultimately yielding the target compound in pure form.

Compound **4g** is Colorless to light yellow liquid ($C_{10}H_{14}O_2$). The crude product showed an R*f* value of approximately 0.37 on TLC (PE/EA=8:2, v/v) when visualized under UV light at 254 nm. Purification was performed by silica gel column chromatography (200-300 mesh) using a gradient eluent system of PE/EA (10:1-1:1, v/v) to afford the pure target compound.

Compound **4h** is a yellow liquid ($C_8H_{11}N$). Purification was performed by silica gel column chromatography (200-300 mesh) using an isocratic eluent of EA to afford the pure target compound.

11. ^{1}H and ^{13}C NMR Spectra

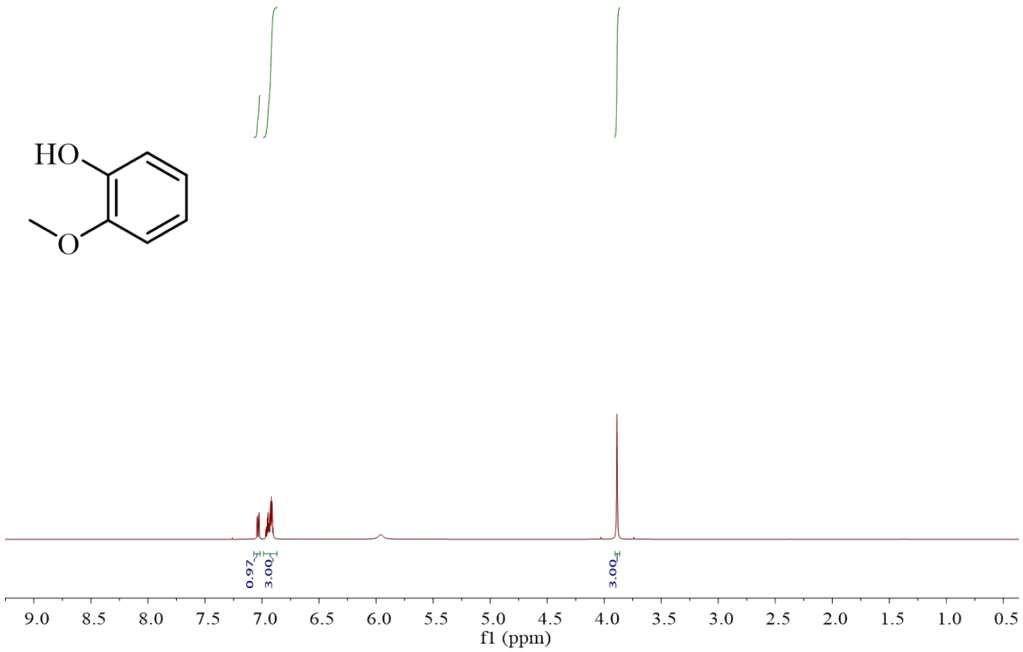

The ^{1}H NMR spectra of **GUA.**^{1}H NMR (500 MHz, Chloroform-*d*) δ 7.07 – 7.02 (m, 1H), 6.99 – 6.87 (m, 3H), 3.89 (s, 3H).

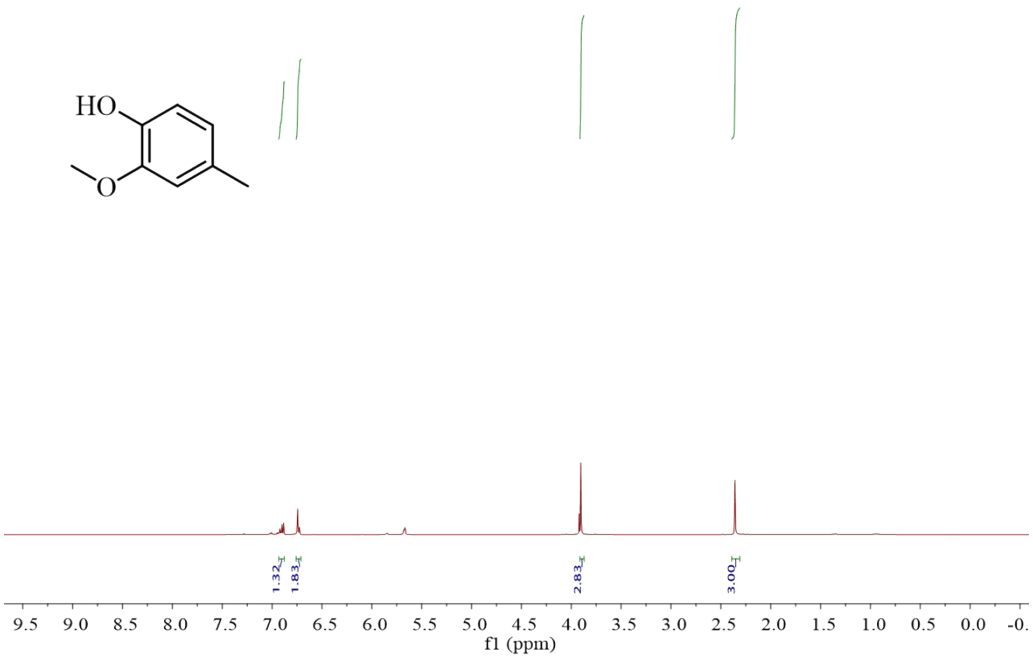

The ^{1}H NMR spectra of **2a.** ^{1}H NMR (500 MHz, Chloroform-*d*) δ 6.93 – 6.88 (m, 1H), 6.73 (d, *J* = 8.1 Hz, 2H), 3.90 (s, 3H), 2.36 (s, 3H).

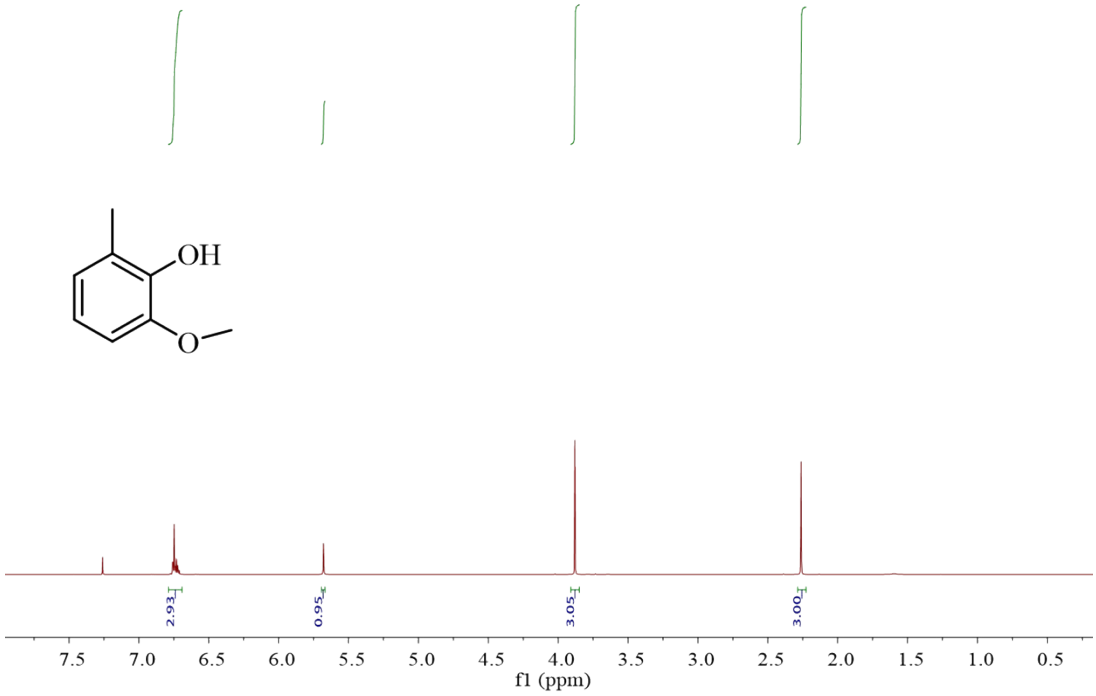

The ^{1}H NMR spectra of **2b**. ^{1}H NMR (500 MHz, Chloroform-*d*) δ 6.79 – 6.69 (m, 3H), 5.68 (s, 1H), 3.88 (s, 3H), 2.26 (s, 3H).

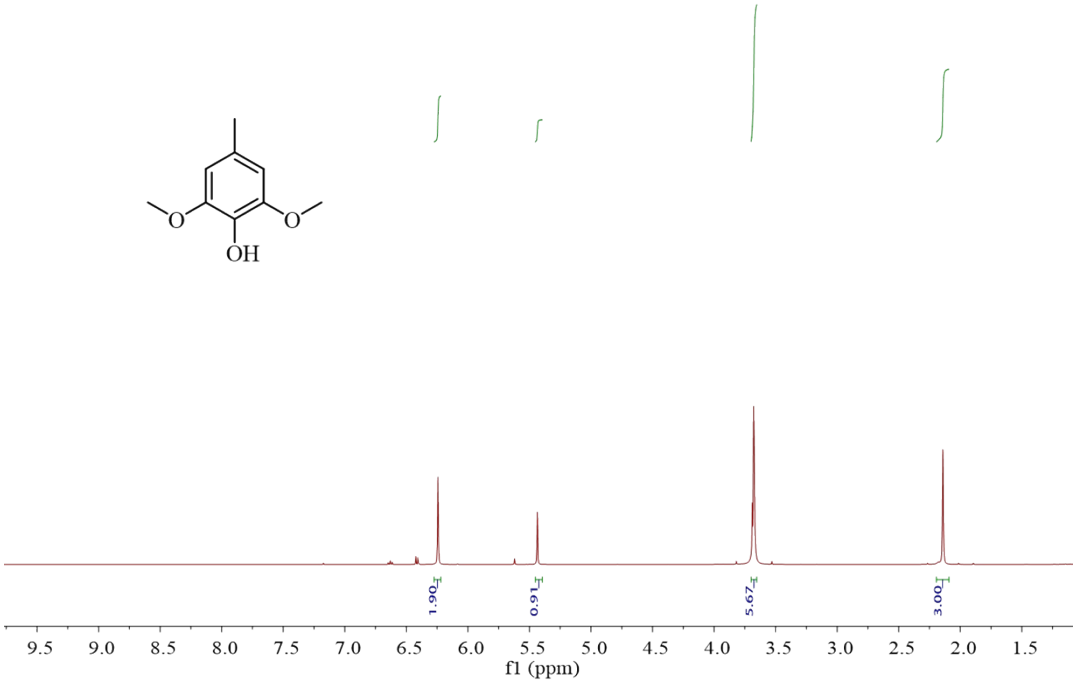

The ^{1}H NMR spectra of **2c.** ^{1}H NMR (500 MHz, Chloroform-*d*) δ 6.24 (s, 2H), 5.44 (s, 1H), 3.68 (d, J = 5.5 Hz, 6H), 2.14 (s, 3H).

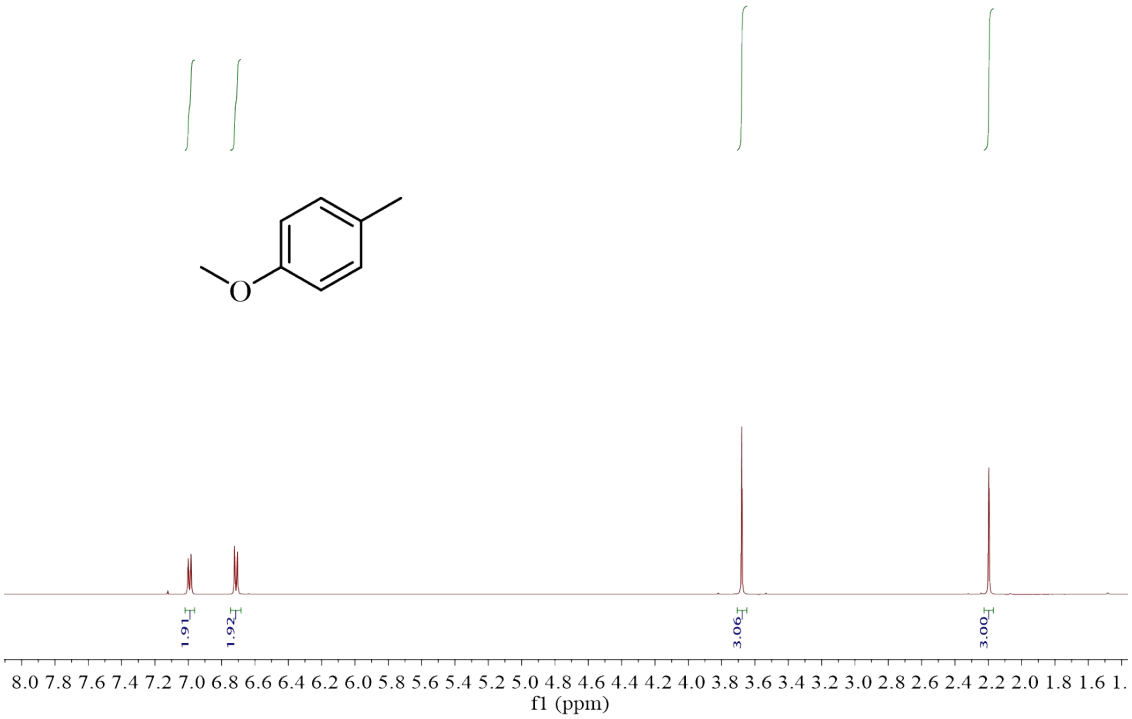

The ^{1}H NMR spectra of **2d**. ^{1}H NMR (500 MHz, Chloroform-*d*) δ 6.99 (d, *J* = 8.4 Hz, 2H), 6.71 (d, *J* = 8.6 Hz, 2H), 3.68 (s, 3H), 2.20 (s, 3H).

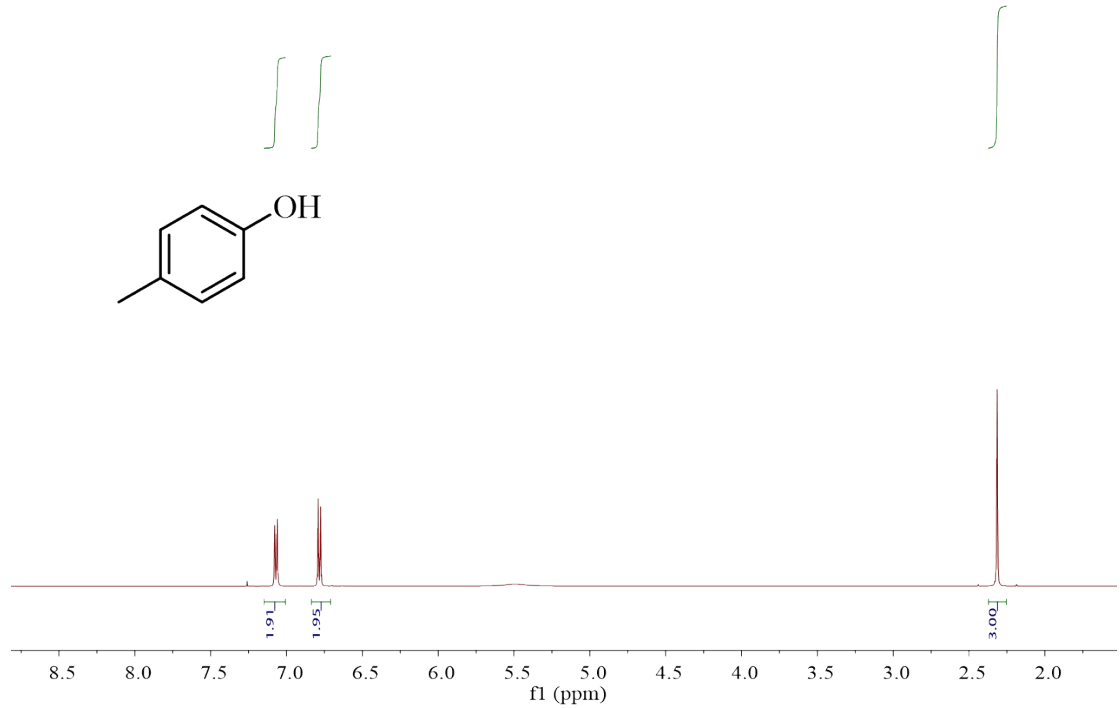

The ^{1}H NMR spectra of **2e**. ^{1}H NMR (500 MHz, Chloroform-*d*) δ 7.07 (d, *J* = 8.3 Hz, 2H), 6.84 – 6.71 (m, 2H), 2.31 (s, 3H).

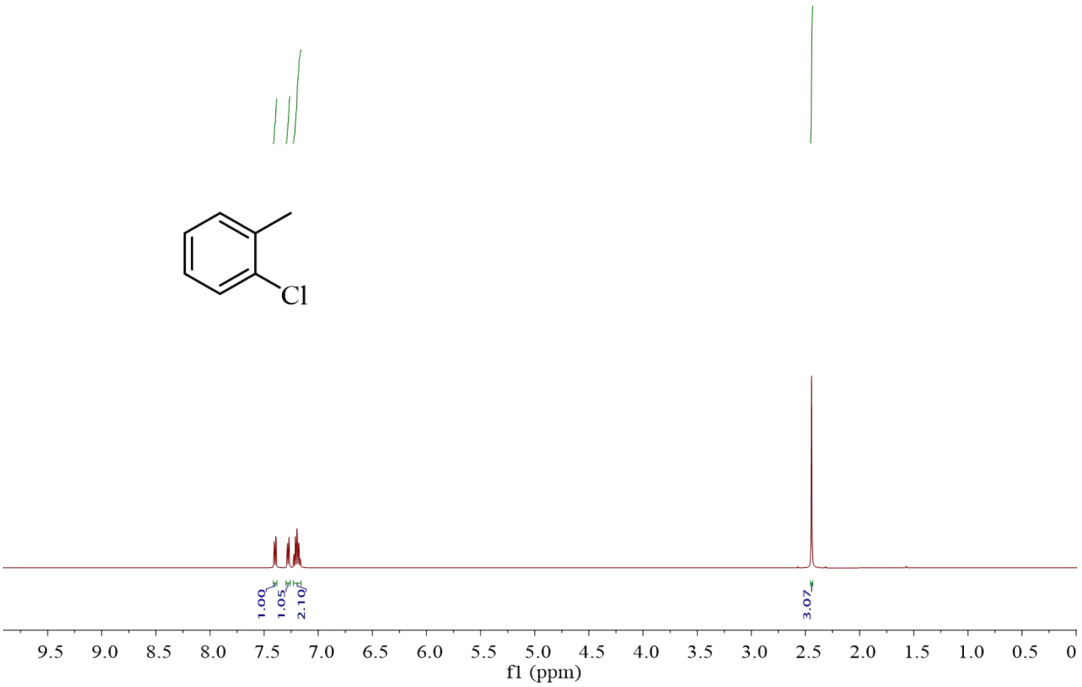

The ^{1}H NMR spectra of **2g**. ^{1}H NMR (500 MHz, Chloroform-*d*) δ 7.40 (dd, *J* = 7.6, 1.7 Hz, 1H), 7.30 – 7.26 (m, 1H), 7.20 (pd, *J* = 7.4, 1.8 Hz, 2H), 2.44 (s, 3H).

The ^{1}H NMR spectra of **2h**. ^{1}H NMR (500 MHz, Chloroform-*d*) δ 7.24 – 7.16 (m, 3H), 7.11 – 7.06 (m, 1H), 2.37 (s, 3H).

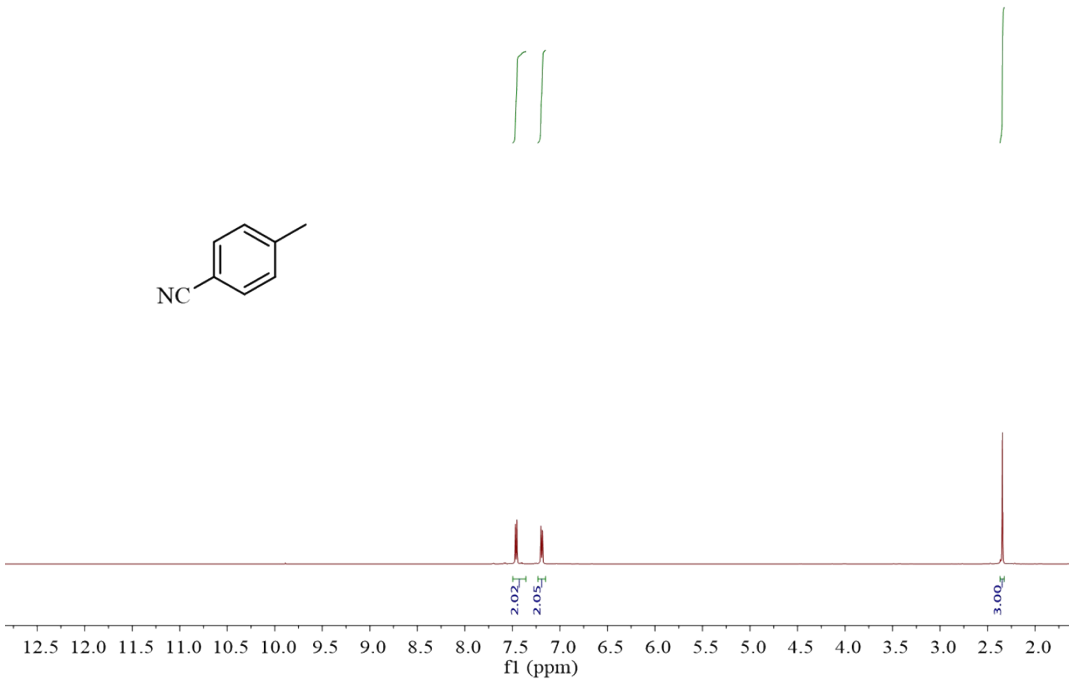

The ^{1}H NMR spectra of **2l.** ^{1}H NMR (500 MHz, Chloroform-*d*) δ 7.46 (d, *J* = 8.1 Hz, 2H), 7.19 (d, *J* = 7.9 Hz, 2H), 2.34 (s, 3H).

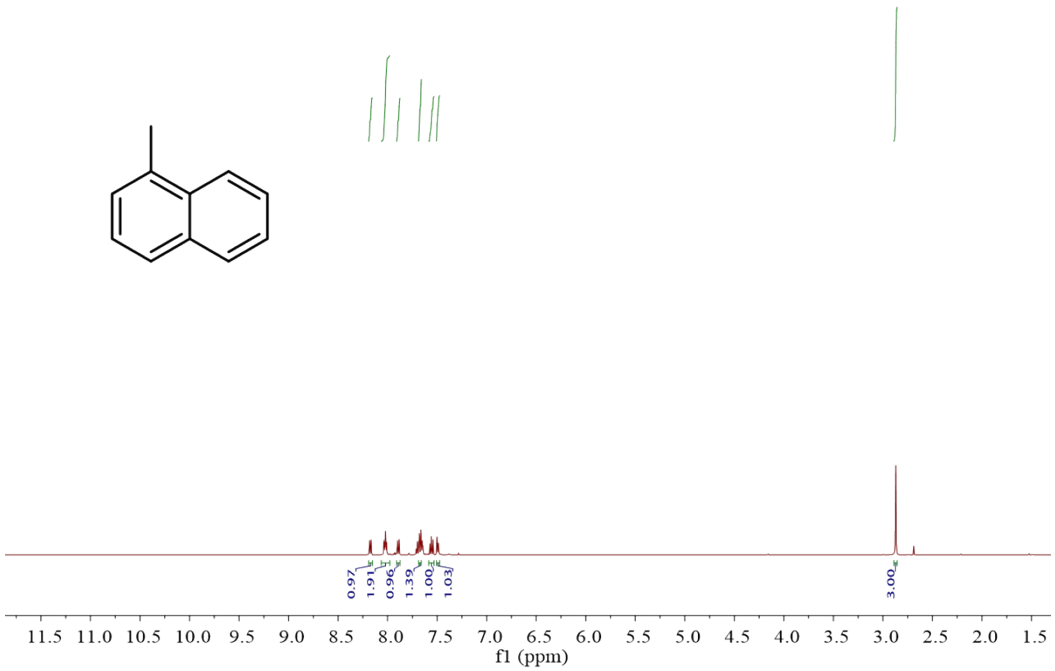

The ^{1}H NMR spectra of **2m**. ^{1}H NMR (500 MHz, Chloroform-*d*) δ 8.18 (dd, *J* = 8.5, 1.3 Hz, 1H), 8.02 (ddd, *J* = 6.4, 4.8, 2.4 Hz, 2H), 7.89 (d, *J* = 8.2 Hz, 1H), 7.72 – 7.67 (m, 1H), 7.56 (dd, *J* = 8.2, 7.0 Hz, 1H), 7.50 (d, *J* = 7.0 Hz, 1H), 2.87 (d, *J* = 1.3 Hz, 3H).

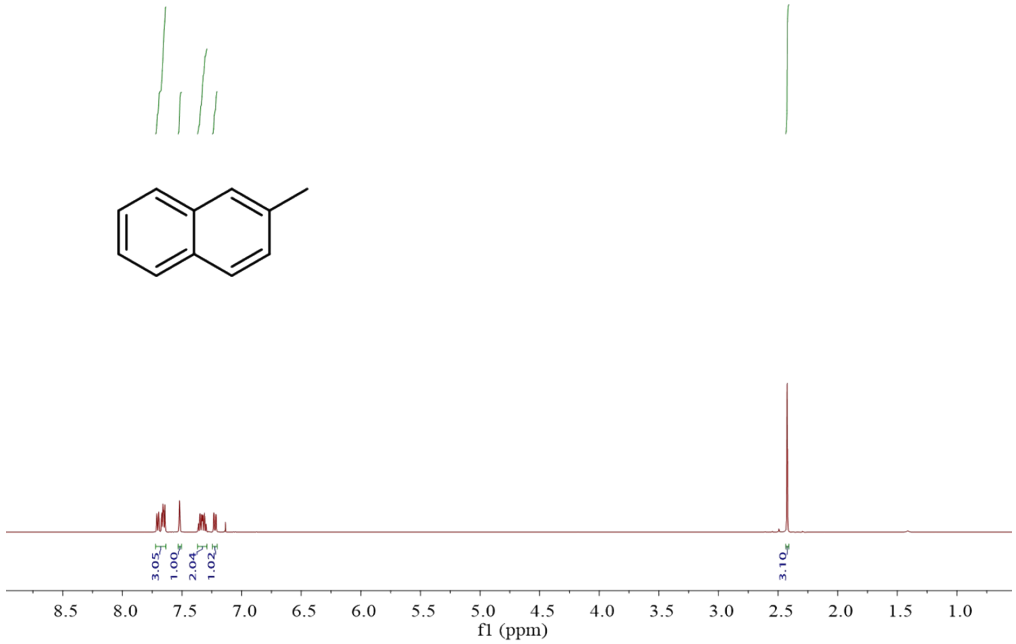

The ^{1}H NMR spectra of **2n**. ^{1}H NMR (500 MHz, Chloroform-*d*) δ 7.72 – 7.63 (m, 3H), 7.52 (s, 1H), 7.37 – 7.29 (m, 2H), 7.22 (dd, *J* = 8.3, 1.7 Hz, 1H), 2.42 (s, 3H).

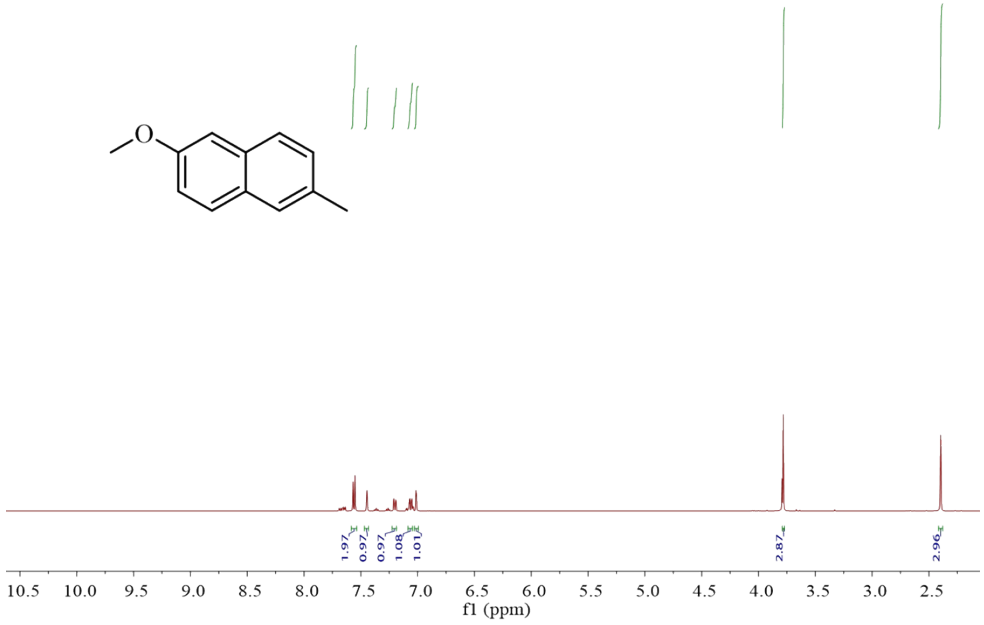

The ^{1}H NMR spectra of **2o.** ^{1}H NMR (500 MHz, Chloroform-*d*) δ 7.56 (d, *J* = 8.7 Hz, 2H), 7.45 (d, *J* = 2.0 Hz, 1H), 7.20 (dd, *J* = 8.4, 1.7 Hz, 1H), 7.08 – 7.04 (m, 1H), 7.01 (d, *J* = 2.6 Hz, 1H), 3.78 (s, 3H), 2.40 (s, 3H).

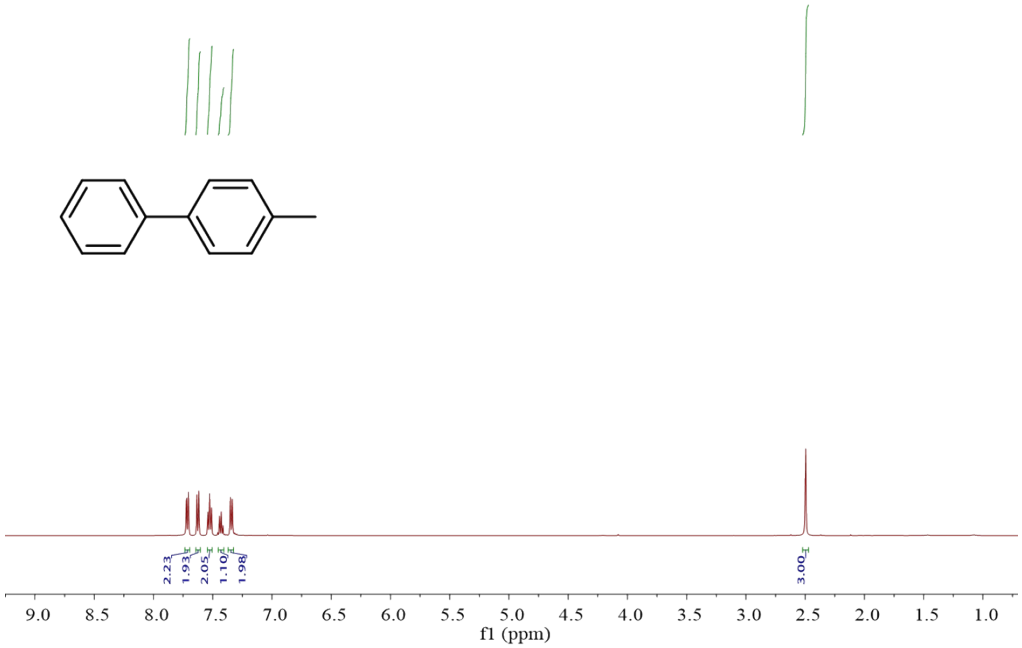

The ^{1}H NMR spectra of **2p.** ^{1}H NMR (500 MHz, Chloroform-*d*) δ 7.71 (d, *J* = 6.9 Hz, 2H), 7.63 (d, *J* = 8.2 Hz, 2H), 7.53 (t, *J* = 7.8 Hz, 2H), 7.43 (t, *J* = 7.4 Hz, 1H), 7.34 (d, *J* = 8.1 Hz, 2H), 2.50 (s, 3H).

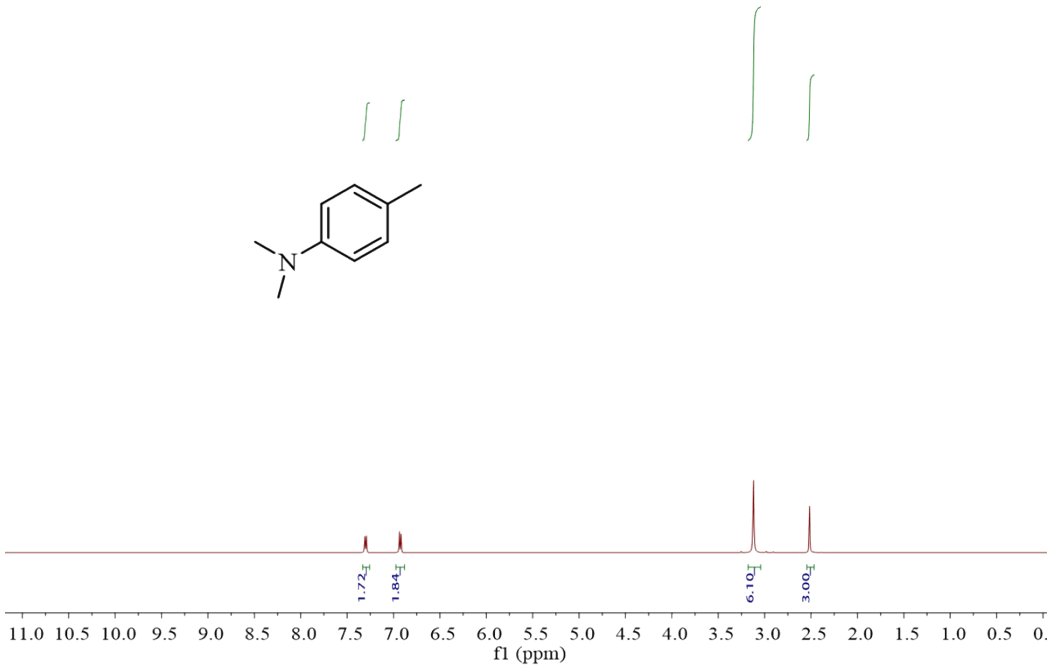

The ^{1}H NMR spectra of **2q**. ^{1}H NMR (500 MHz, Chloroform-*d*) δ 7.30 (d, *J* = 8.7 Hz, 2H), 6.93 (d, *J* = 8.8 Hz, 2H), 3.12 (s, 6H), 2.52 (s, 3H).

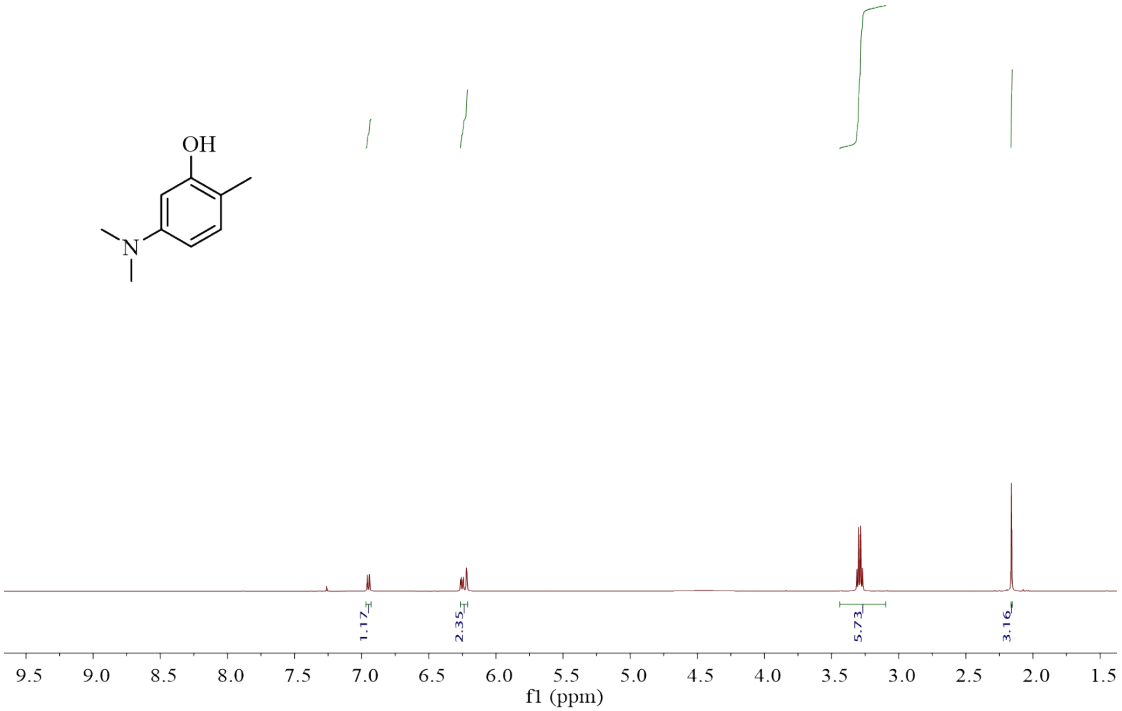

The ^{1}H NMR spectra of **2r**. ^{1}H NMR (500 MHz, Chloroform-*d*) δ 6.97 – 6.93 (m, 1H), 6.26 – 6.21 (m, 2H), 3.29 (q, *J* = 7.1 Hz, 6H), 2.16 (s, 3H).

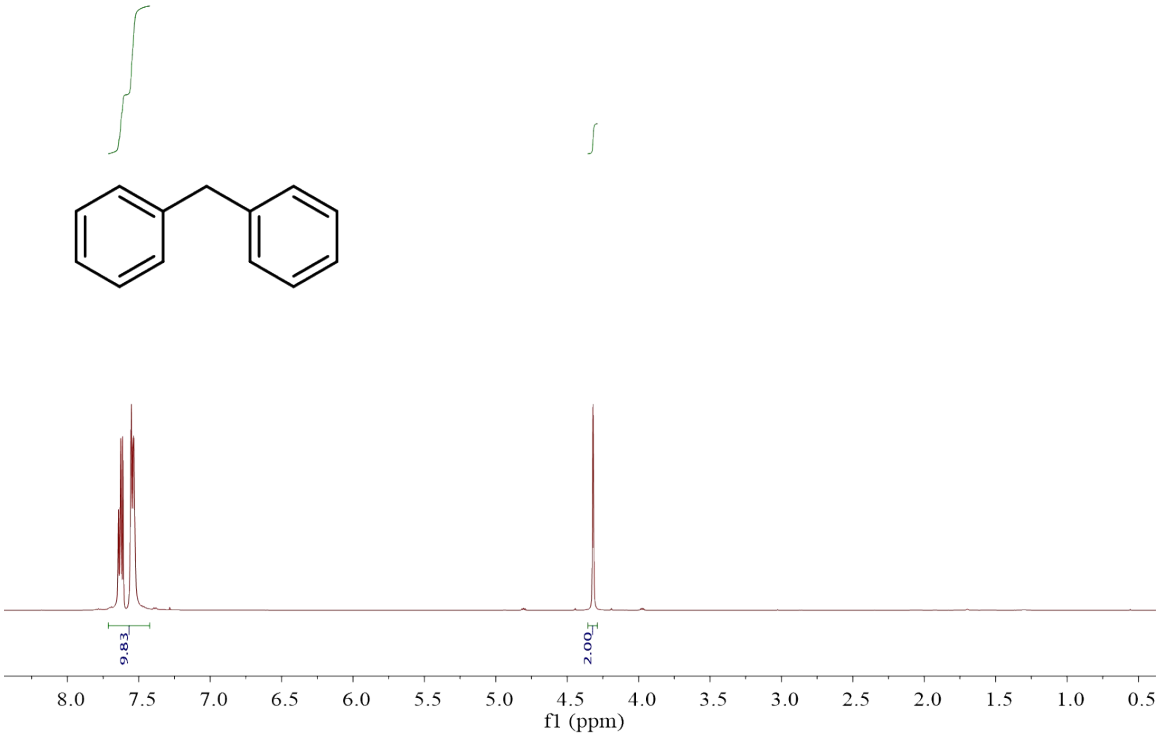

The ^{1}H NMR spectra of **4a**. ^{1}H NMR (500 MHz, Chloroform-*d*) δ 7.71-7.42 (m, 10H), 4.32 (s, 2H).

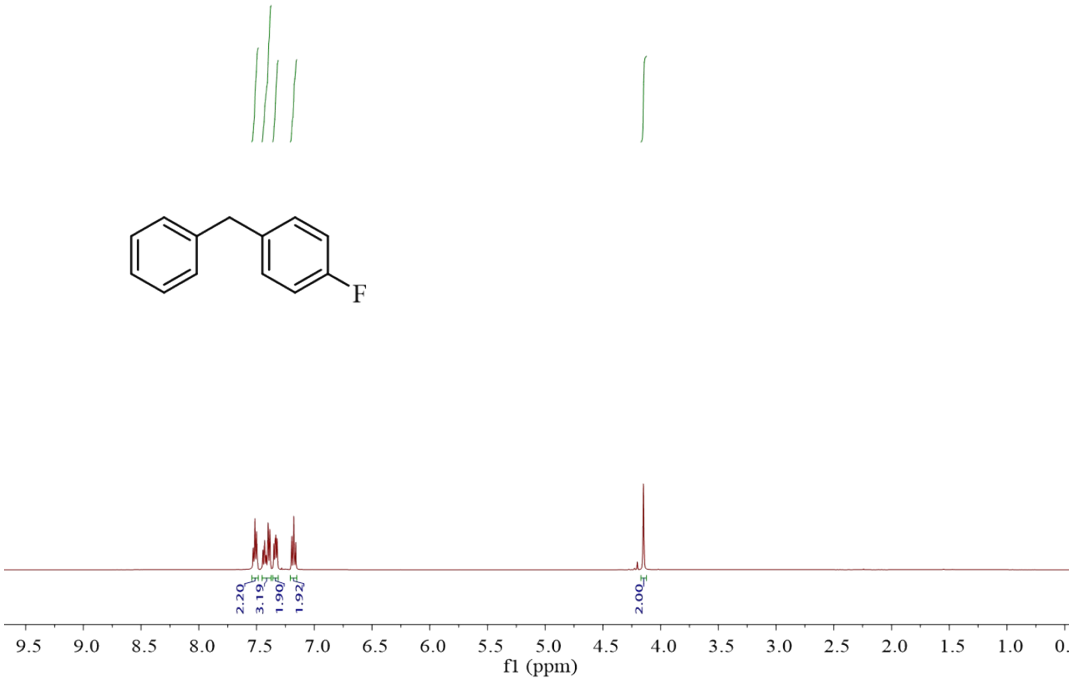

The ^{1}H NMR spectra of **4b**. ^{1}H NMR (500 MHz, Chloroform-*d*) δ 7.51 (t, *J* = 7.7 Hz, 2H), 7.45 – 7.37 (m, 3H), 7.34 (dd, *J* = 8.5, 5.5 Hz, 2H), 7.21 – 7.15 (m, 2H), 4.15 (s, 2H).

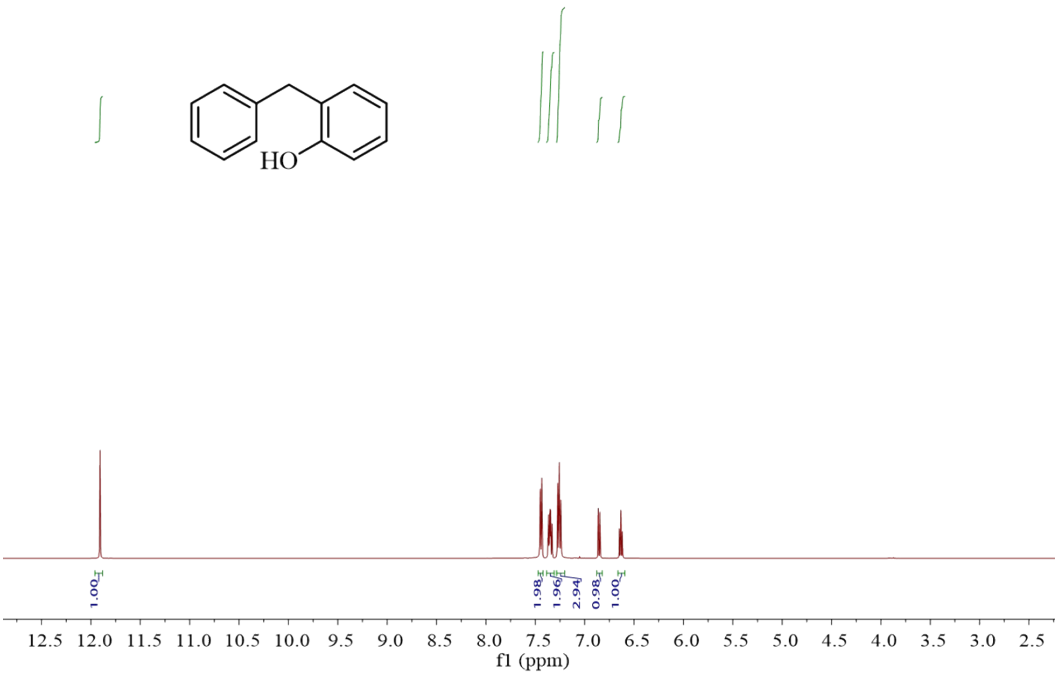

The ^{1}H NMR spectra of **4c.** ^{1}H NMR (500 MHz, Chloroform-*d*) δ 11.91 (s, 1H), 7.47 – 7.42 (m, 2H), 7.39 – 7.31 (m, 2H), 7.26 (d, *J* = 8.2 Hz, 3H), 6.85 (dd, *J* = 8.4, 1.2 Hz, 1H), 6.63 (ddd, *J* = 8.3, 7.2, 1.2 Hz, 1H).

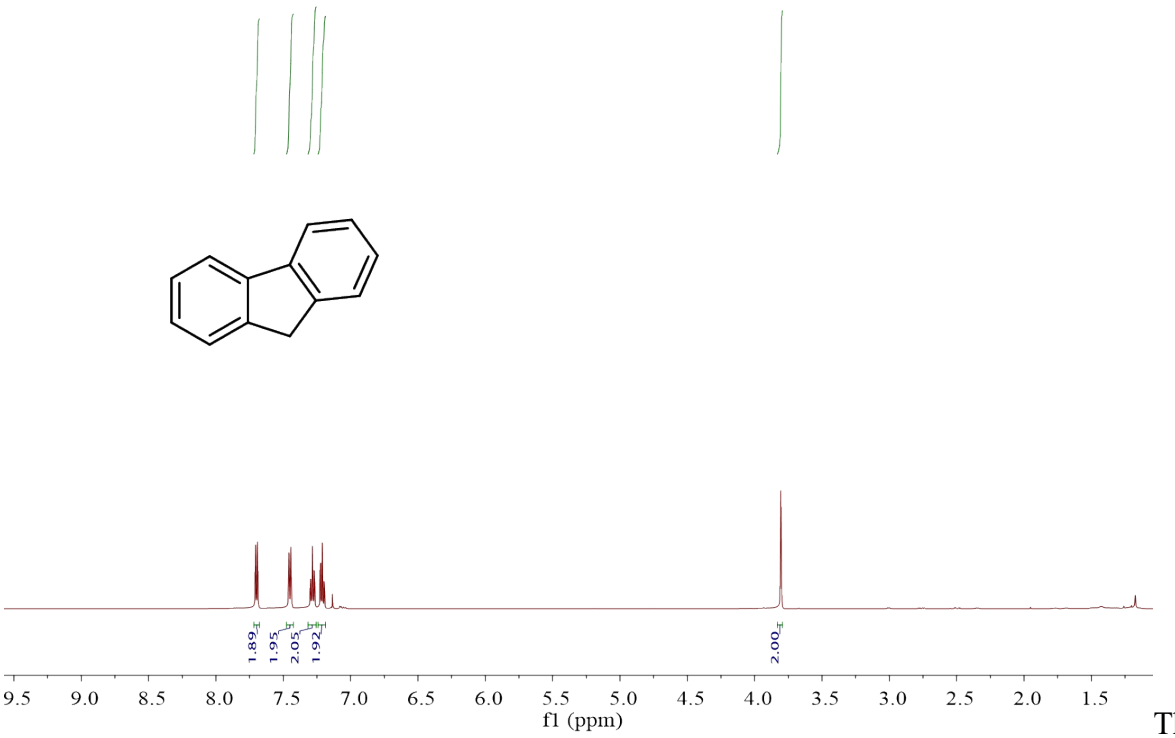

The ^{1}H NMR spectra of **4d.** ^{1}H NMR (500 MHz, Chloroform-*d*) δ 7.70 (d, *J* = 7.6 Hz, 2H), 7.45 (d, *J* = 7.5 Hz, 2H), 7.32 – 7.25 (m, 2H), 7.21 (td, *J* = 7.4, 1.2 Hz, 2H), 3.81 (s, 2H).

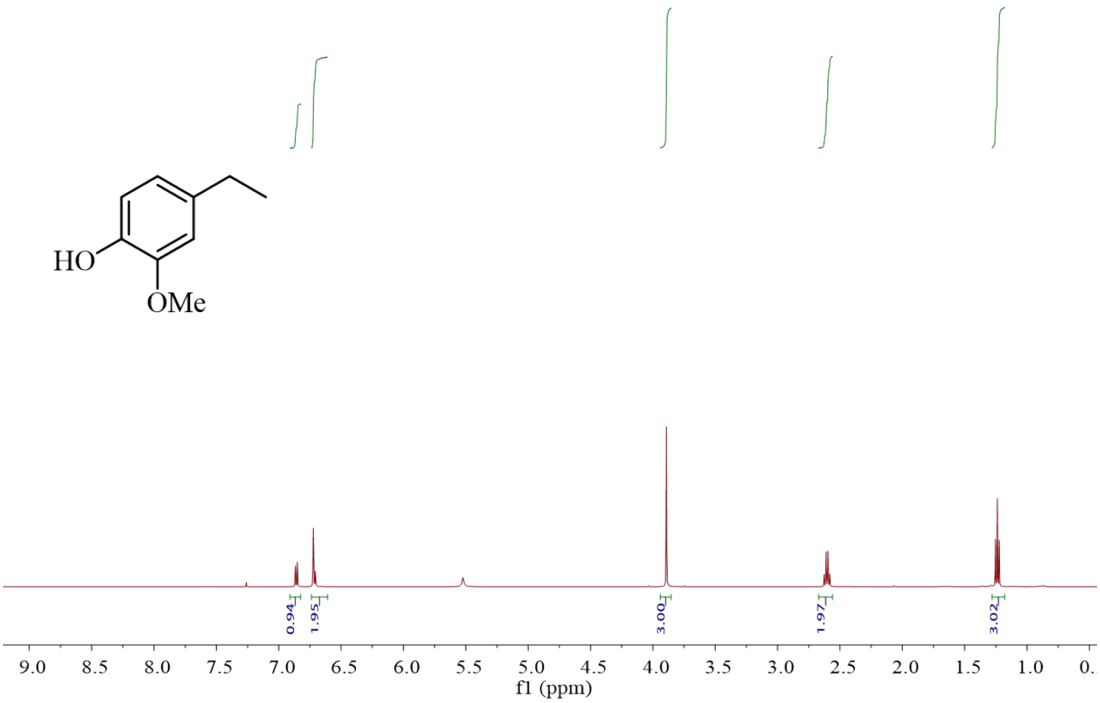

The ^{1}H NMR spectra of **4e**. ^{1}H NMR (500 MHz, Chloroform-*d*) δ 6.86 (d, *J* = 7.8 Hz, 1H), 6.71 (d, *J* = 7.8 Hz, 2H), 3.89 (s, 3H), 2.60 (q, *J* = 7.6 Hz, 2H), 1.24 (t, *J* = 7.6 Hz, 3H).

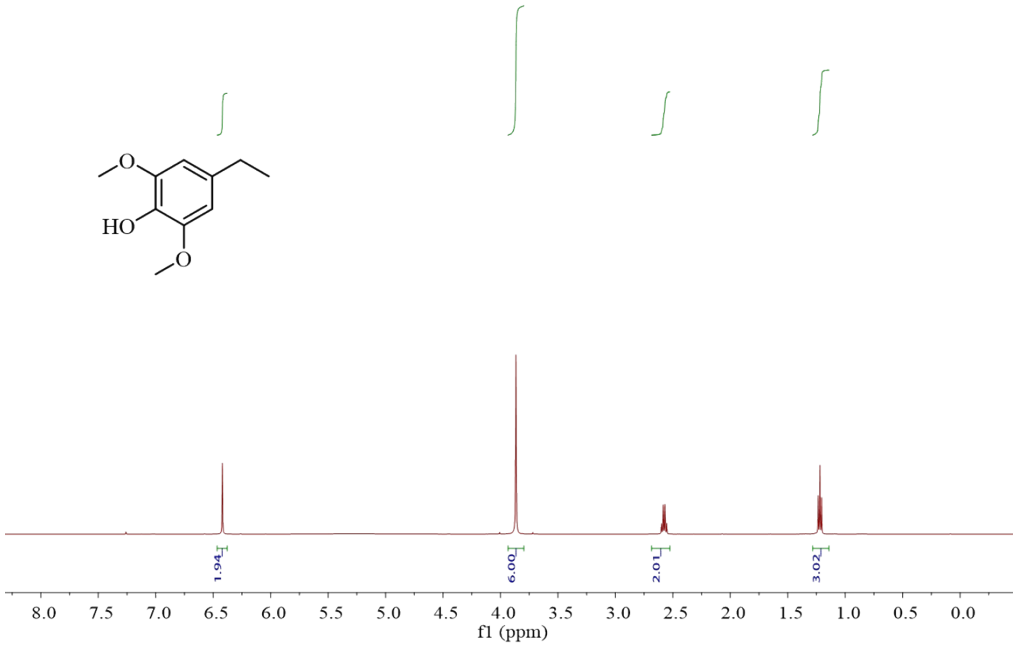

The ^{1}H NMR spectra of **4f**. ^{1}H NMR (500 MHz, Chloroform-*d*) δ 6.42 (s, 2H), 3.87 (s, 6H), 2.58 (q, *J* = 7.6 Hz, 2H), 1.22 (t, *J* = 7.6 Hz, 3H).

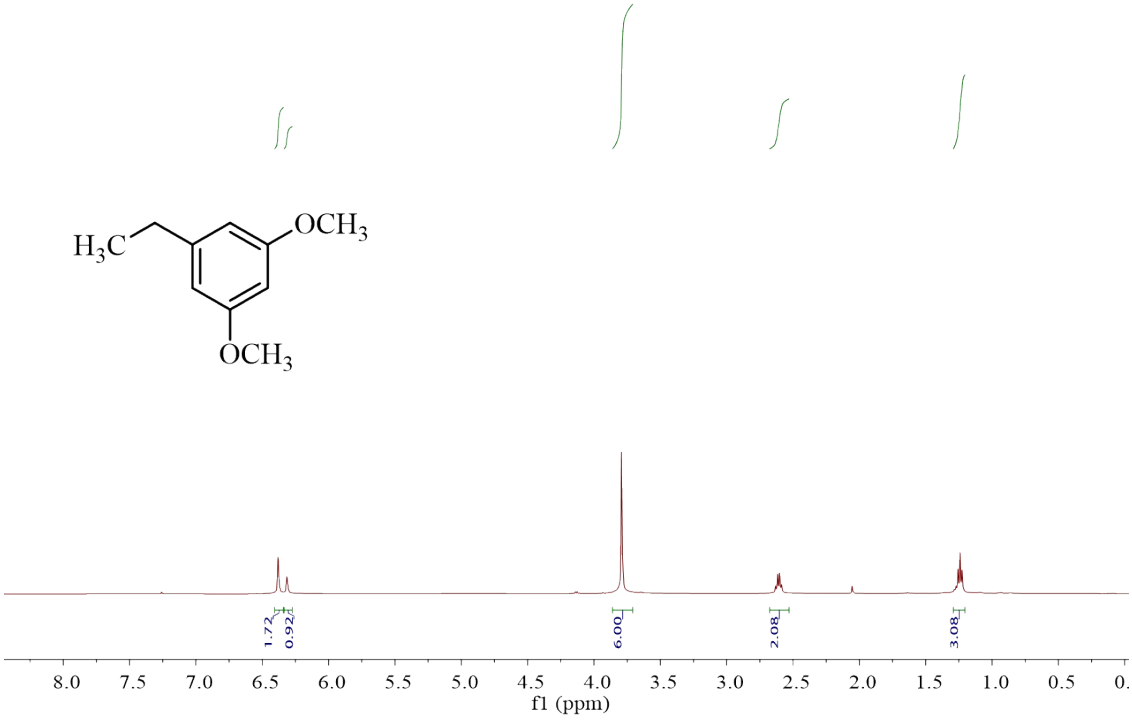

The ^{1}H NMR spectra of **4g**. ^{1}H NMR (500 MHz, Chloroform-*d*) δ 6.38 (d, *J* = 2.2 Hz, 2H), 6.31 (d, *J* = 2.6 Hz, 1H), 3.79 (s, 6H), 2.61 (q, *J* = 7.6 Hz, 2H), 1.24 (t, *J* = 7.6 Hz, 3H).

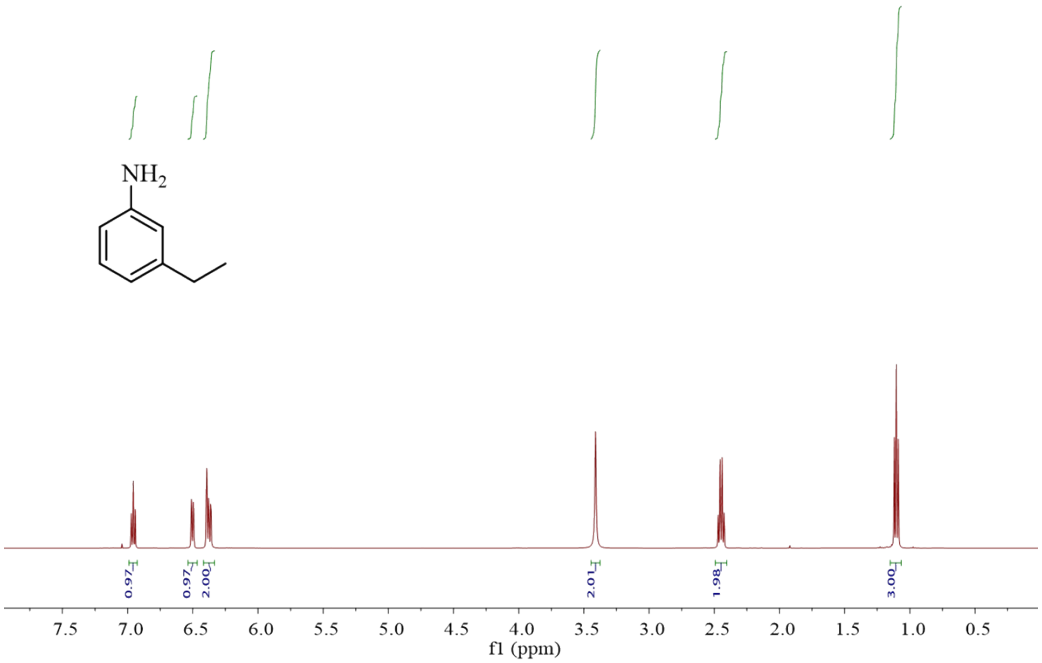

The ^{1}H NMR spectra of **4h.** ^{1}H NMR (500 MHz, Chloroform-*d*) δ 6.96 (td, *J* = 7.7, 1.3 Hz, 1H), 6.50 (d, *J* = 7.6 Hz, 1H), 6.42 – 6.33 (m, 2H), 3.41 (s, 2H), 2.45 (q, *J* = 7.6 Hz, 2H), 1.10 (td, *J* = 7.6, 1.6 Hz, 3H).

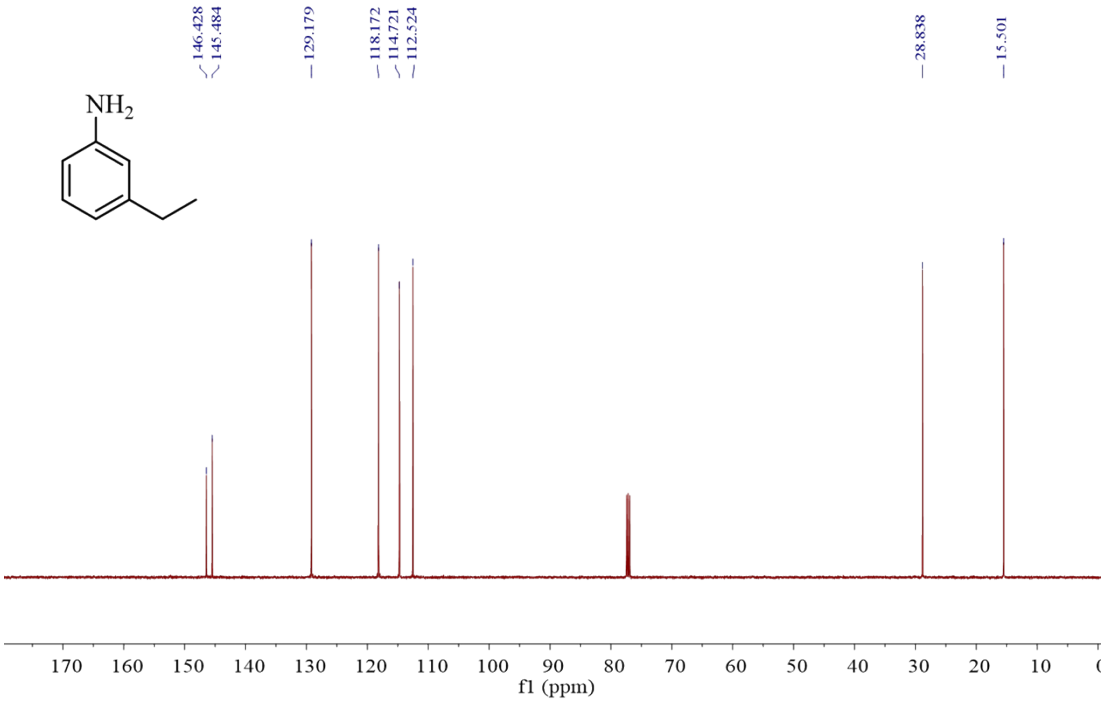

The ^{13}C NMR spectra of **4h.**